

Vortex Methods for Direct Numerical Simulation of Three-Dimensional Bluff Body Flows: Application to the Sphere at $Re = 300, 500$, and 1000

P. Ploumhans,^{*,1} G. S. Winckelmans,^{*,2} J. K. Salmon,[†] A. Leonard,[‡] and M. S. Warren[§]

^{*}*Center for Systems Engineering and Applied Mechanics (CESAME), Department of Mechanical Engineering, Université catholique de Louvain, 1348 Louvain-la-Neuve, Belgium;* [†]*Digital Island, Thousand Oaks, California 91360;* [‡]*Graduate Aeronautical Laboratories, California Institute of Technology, Pasadena, California 91125;* and [§]*Los Alamos National Laboratory, Los Alamos, New Mexico 87545*
E-mail: ploumhan@term.ucl.ac.be, gsu@term.ucl.ac.be, jsalmon@thesalmons.org,
tony@calcit.caltech.edu, and mswarren@lanl.gov

Received May 1, 2001; revised January 11, 2002

Recent contributions to the 3-D vortex methods are presented. Following Cottet, the particles strength exchange (PSE) scheme for diffusion is modified in the vicinity of solid boundaries to avoid a spurious vorticity flux and to enforce a zero-normal component of vorticity during the convection/PSE step. The vortex sheet algorithm used to enforce the no-slip boundary condition through a vorticity flux at the boundary and the technique used to perform accurate redistributions in the presence of bodies of general geometry are extended from their 2-D counterpart. To perform simulations with nonuniform resolution, a mapping of the redistribution lattice is used. Computational efficiency is attained through the use of parallel tree codes based on multipole expansions of vortex particles and of vortex panels. The method is validated, by comparisons with other authors' results, on the flow past a sphere at $Re = 300$. It is then applied to compute the flow at $Re = 500$ and 1000 . © 2002 Elsevier Science (USA)

Key Words: vortex method; particle method; viscous flow; particle redistribution; 3D flow; sphere.

1. INTRODUCTION

In the past two decades, significant developments in the field of vortex methods have made them well suited to perform high-resolution simulations of the incompressible Navier–Stokes equations in unbounded domains. These developments include fast algorithms using

¹ New address: Free Field Technologies SA, Place de l'Université, 16, 1348 Louvain-la-Neuve, Belgium.

² Fax: 00-32-(0)-10-452692.

multipole expansions (Greengard and Rohklin [11], Barnes and Hut [2]) and active error control (so that the error induced by the use of multipole expansions is less than a prescribed tolerance) (Salmon and Warren [40], Winckelmans *et al.* [45, 47]), accurate treatment of viscous effects using the particle strength exchange scheme (PSE; Degond and Mas-Gallic [9], Mas-Gallic [27], Winckelmans and Leonard [44]), accurate enforcement of the viscous boundary condition (Koumoutsakos *et al.* [17], Cottet and Koumoutsakos [7], Leonard *et al.* [21], Benhaddouch [4], Ploumhans *et al.* [34], Ploumhans and Winckelmans [35, 36]), use of a mapping to allow one to perform simulations with nonuniform spatial resolution (Cottet *et al.* [6, 8], Ould Salihi [32], Cottet and Koumoutsakos [7], Ploumhans and Winckelmans [35, 36]), and a symmetrized PSE (Ploumhans and Winckelmans [35, 36]) and capability of performing an accurate particle redistribution in the presence of a boundary that crosses the redistribution lattice in an arbitrary way, thus allowing for bodies of general shape (Ploumhans *et al.* [34], Ploumhans and Winckelmans [35, 36]). These developments have all been implemented in 2-D, making it possible to compute flows past bluff bodies of general geometries [35, 36].

The complexity of three-dimensional flows makes it necessary to use a high number of computational elements: in practice, this also requires parallel algorithms. Part of the developments mentioned above have already been implemented in 3-D, enabling computation of 3-D viscous flows without boundaries on parallel computers, with an $\mathcal{O}(N \log N)$ computational cost (Winckelmans *et al.* [45, 47]).

In this paper, we present several developments aimed at the high-resolution simulations of flows past 3-D bluff bodies of general geometry. A fast parallel boundary element solver (that solves the system of equations involved in the boundary condition enforcement in $\mathcal{O}(M \log M)$ operations per iteration) is coupled with the 3-D code previously developed by Winckelmans *et al.* [45–47] and by Ploumhans *et al.* [34]. It is here complemented by the 3-D extension of the general redistribution technique presented in [35, 36], and by the use of a 3-D mapping. This enables the performing of direct numerical simulations (DNS) of high Reynolds number 3-D flows past bluff bodies of arbitrary shape, using a fast parallelized vortex method with nonuniform resolution.

The paper is organized into the following parts. The basic equations (Section 2), the vortex method (Section 3), a presentation of the techniques used to measure the forces acting on the body (Section 4), and the validation of the method on the flow past a sphere at $Re = 300, 500$, and 1000 (Section 5).

2. THE BASIC EQUATIONS FOR 3-D FLOWS

Three-dimensional incompressible flows are governed by the vorticity equation

$$\frac{D\boldsymbol{\omega}}{Dt} = \frac{\partial \boldsymbol{\omega}}{\partial t} + \mathbf{u} \cdot \nabla \boldsymbol{\omega} = (\nabla \mathbf{u}) \cdot \boldsymbol{\omega} + \nu \nabla^2 \boldsymbol{\omega}, \quad (1)$$

where $\mathbf{u}(\mathbf{x}, t)$ is the velocity field, ν is the kinematic viscosity, and $\boldsymbol{\omega} = \nabla \times \mathbf{u}$ is the vorticity. In viscous flows, one must satisfy the no-slip boundary condition on solid surfaces. In the vorticity formulation, Eq. (1), boundary conditions on the three components of the vorticity are needed: a Dirichlet condition on the normal component of $\boldsymbol{\omega}$ (Saffman [37], Cottet [5]),

$$\omega_n \triangleq \boldsymbol{\omega} \cdot \mathbf{n} = 0 \quad (2)$$

(as the tangential derivatives of the velocity vanish at the wall), and a Neumann condition on the two tangential components of ω (expressing the cancellation of the tangential components of the slip velocity at the wall). The velocity can be expressed as

$$\mathbf{u} = \nabla \times \psi + \mathbf{U}_\infty, \quad (3)$$

with \mathbf{U}_∞ the free stream velocity and ψ the stream function related to ω by

$$\nabla^2 \psi = -\omega. \quad (4)$$

3. THE VORTEX METHOD FOR 3-D FLOWS

In the present method, the vorticity field is represented by a set of N Lagrangian, vector-valued particles,

$$\tilde{\omega}(\mathbf{x}, t) = \sum_{i=1}^N \zeta_i(\mathbf{x} - \mathbf{x}_i) \alpha_i, \quad (5)$$

where the particles have positions $\mathbf{x}_i(t)$ and vector strengths α_i that have units of circulation times length: $\alpha_i = \int_{V_i} \omega dV \triangleq \omega_i V_i$, with V_i the volume of fluid associated with the particle i . The distribution function, ζ_i , associated with each particle is defined by

$$\zeta_i(\mathbf{x}) = \frac{1}{\sigma_i^3} \zeta\left(\frac{|\mathbf{x}|}{\sigma_i}\right), \quad (6)$$

where σ_i is the smoothing parameter. There are many possible choices for the function ζ (see, e.g., Leonard [23], Winckelmans and Leonard [44]). The Gaussian distribution is here used throughout:

$$\zeta(\rho) = \frac{1}{(2\pi)^{3/2}} \exp\left(-\frac{\rho^2}{2}\right). \quad (7)$$

The velocity field is computed from Eq. (5) as the curl of the stream function which solves $\nabla^2 \tilde{\psi} = -\tilde{\omega}$. Defining $G(\rho)$ such that

$$\nabla^2 G(\rho) = -\zeta(\rho), \quad (8)$$

one obtains

$$\tilde{\psi}(\mathbf{x}, t) = \sum_{i=1}^N G_i(\mathbf{x} - \mathbf{x}_i) \alpha_i, \quad (9)$$

where $G_i(\mathbf{x} - \mathbf{x}_i) = G(|\mathbf{x} - \mathbf{x}_i|/\sigma_i)/\sigma_i$. The velocity \mathbf{u} is obtained as

$$\mathbf{u}(\mathbf{x}, t) = - \sum_{j=1}^N \frac{q(|\mathbf{x} - \mathbf{x}_j|/\sigma_j)}{|\mathbf{x} - \mathbf{x}_j|^3} (\mathbf{x} - \mathbf{x}_j) \times \alpha_j, \quad (10)$$

with $q(\rho) = \int_0^\rho \zeta(s) s^2 ds$. For the Gaussian smoothing, $G(\rho) = \text{erf}(\rho/\sqrt{2})/(4\pi\rho)$ and $q(\rho) = (\text{erf}(\rho/\sqrt{2}) - \sqrt{2/\pi} \rho \exp(-\rho^2/2))/(4\pi)$, where $\text{erf}(s) = \frac{2}{\sqrt{\pi}} \int_0^s \exp(-v^2) dv$.

It is worth noting that the particle field, Eq. (5), is not generally divergence free. Thus, a basis that is not divergence free is used to represent the vorticity field (Winckelmans and Leonard [44], Leonard *et al.* [21], Cottet [5]). The stream function, Eq. (9), is also not

generally divergence free, as $\nabla^2 \tilde{\psi} = -\tilde{\omega}$ is solved with $\tilde{\omega}$ not generally divergence free. The velocity, \mathbf{u} , is always divergence free because it is the curl of a field. As a convention, a “tilde” is used to refer to the particle fields: Eqs. (5) and (9). We reserve the notation ω for the divergence-free vorticity field $\omega = \nabla \times \mathbf{u}$. When $\tilde{\omega}$ and ω differ substantially, a relaxation scheme can be used, where the particle weights are reset after redistribution so as to best represent ω (Winckelmans and Leonard [44], Cottet [5], Leonard *et al.* [21]).

The way to handle viscous boundaries in the 2-D vortex method was originally developed by Koumoutsakos *et al.* [17]. This method was later modified to make it more accurate, better suited to the computation of flows past bodies of general geometry, and conservative (Leonard *et al.* [21], Ploumhans *et al.* [34], Ploumhans and Winckelmans [35, 36]). It has also been extended to 3-D (Ploumhans *et al.* [34]). A typical time step, Δt , of the 3-D vortex method is divided into two substeps:

- In *substep 1*, the local velocity is computed and integrated to convect the particles (Section 3.1). Their strength is updated to account for the stretching (Section 3.1) and for the diffusion (Section 3.2). The diffusion is treated with a modified particle strength exchange (PSE) scheme, which guarantees a zero vorticity flux and a zero-normal component of the vorticity at the solid boundary during substep 1. A second-order Adams–Bashforth scheme is used for the time integration. After this substep, a slip velocity, $\Delta \mathbf{U}_{\text{slip}}$, is present at the solid boundary. Algorithmically, substep 1 is expressed as

$$\mathbf{x}_i^{n+1} = \mathbf{x}_i^n + \Delta t \left(\frac{3}{2} \mathbf{u}_i(\mathbf{x}^n, \alpha^n) - \frac{1}{2} \mathbf{u}_i(\mathbf{x}^{n-1}, \alpha^{n-1}) \right), \quad (11)$$

$$\begin{aligned} \alpha_i^{*,n+1} = \alpha_i^n + \Delta t & \left(\frac{3}{2} \left(\frac{d\alpha_i}{dt} \Big|_{\text{st}} (\mathbf{x}^n, \alpha^n) + \frac{d\alpha_i}{dt} \Big|_{\text{PSE}} (\mathbf{x}^n, \alpha^n) \right) \right. \\ & \left. - \frac{1}{2} \left(\frac{d\alpha_i}{dt} \Big|_{\text{st}} (\mathbf{x}^{n-1}, \alpha^{n-1}) + \frac{d\alpha_i}{dt} \Big|_{\text{PSE}} (\mathbf{x}^{n-1}, \alpha^{n-1}) \right) \right). \end{aligned} \quad (12)$$

- In *substep 2*, the vector-valued vortex sheet, $\Delta \gamma$, necessary on the body surface to cancel the slip velocity generated by substep 1 is computed (Section 3.3). This vortex sheet corresponds to a vorticity flux that must be emitted during a time Δt (Section 3.4):

$$\alpha_i^{n+1} = \alpha_i^{*,n+1} + \Delta t \left(\frac{3}{2} \frac{d\alpha_i}{dt} \Big|_{\text{wall}} (\mathbf{x}^{n+1}, \alpha^{*,n+1}) - \frac{1}{2} \frac{d\alpha_i}{dt} \Big|_{\text{wall}} (\mathbf{x}^n, \alpha^{*,n}) \right). \quad (13)$$

Also, a redistribution scheme must be applied every few steps (Section 3.5) to maintain spatial uniformity of the particle distribution and thus maintain the second-order spatial accuracy of the method. After each particle redistribution, the new time step is done using a second-order Runge–Kutta scheme (Euler predictor, trapezoidal rule corrector). Such a time step is as follows:

(a) Euler predictor,

$$\mathbf{x}_i^{n+1/2} = \mathbf{x}_i^n + \Delta t \mathbf{u}_i(\mathbf{x}^n, \alpha^n), \quad (14)$$

$$\alpha_i^{*,n+1/2} = \alpha_i^n + \Delta t \frac{d\alpha_i}{dt} \Big|_{\text{st+PSE}} (\mathbf{x}^n, \alpha^n), \quad (15)$$

$$\alpha_i^{n+1/2} = \alpha_i^{*,n+1/2} + \Delta t \frac{d\alpha_i}{dt} \Big|_{\text{wall}} (\mathbf{x}^{n+1/2}, \alpha^{*,n+1/2}). \quad (16)$$

(b) Trapezoïdal rule corrector,

$$\mathbf{x}_i^{n+1} = \mathbf{x}_i^n + \frac{1}{2} \Delta t (\mathbf{u}_i(\mathbf{x}^n, \boldsymbol{\alpha}^n) + \mathbf{u}_i(\mathbf{x}^{n+1/2}, \boldsymbol{\alpha}^{n+1/2})), \quad (17)$$

$$\boldsymbol{\alpha}_i^{*,n+1} = \boldsymbol{\alpha}_i^n + \frac{1}{2} \Delta t \left(\left. \frac{d\boldsymbol{\alpha}_i}{dt} \right|_{\text{st+PSE}} (\mathbf{x}^n, \boldsymbol{\alpha}^n) + \left. \frac{d\boldsymbol{\alpha}_i}{dt} \right|_{\text{st+PSE}} (\mathbf{x}^{n+1/2}, \boldsymbol{\alpha}^{n+1/2}) \right), \quad (18)$$

$$\boldsymbol{\alpha}_i^{n+1} = \boldsymbol{\alpha}_i^{*,n+1} + \frac{1}{2} \Delta t \left(\left. \frac{d\boldsymbol{\alpha}_i}{dt} \right|_{\text{wall}} (\mathbf{x}^{n+1/2}, \boldsymbol{\alpha}^{*,n+1/2}) + \left. \frac{d\boldsymbol{\alpha}_i}{dt} \right|_{\text{wall}} (\mathbf{x}^{n+1}, \boldsymbol{\alpha}^{*,n+1}) \right). \quad (19)$$

3.1. Convection and Stretching

Particle positions $\mathbf{x}_i(t)$ are governed by the equation

$$\frac{d\mathbf{x}_i}{dt} = \mathbf{u}(\mathbf{x}_i(t), t), \quad (20)$$

with

$$\mathbf{u}(\mathbf{x}_i(t), t) = - \sum_{j=1}^N \frac{q(|\mathbf{x}_i - \mathbf{x}_j|/\sigma_{ij})}{|\mathbf{x}_i - \mathbf{x}_j|^3} (\mathbf{x}_i - \mathbf{x}_j) \times \boldsymbol{\alpha}_j, \quad (21)$$

where $\sigma_{ij}^2 = (\sigma_i^2 + \sigma_j^2)/2$. The use of the symmetrized σ is required for the convection step to best conserve the linear and angular impulse (Leonard [22]). Particle strengths $\boldsymbol{\alpha}_i(t)$ are stretched and rotated according to

$$\left. \frac{d\boldsymbol{\alpha}_i}{dt} \right|_{st} = (\nabla \mathbf{u}(\mathbf{x}_i(t), t)) \cdot \boldsymbol{\alpha}_i(t), \quad (22)$$

where the velocity gradient is obtained by analytically differentiating Eq. (21). This is the so-called *direct scheme*. The fact that

$$(\nabla \mathbf{u}) \cdot \boldsymbol{\omega} = (\nabla \mathbf{u})^T \cdot \boldsymbol{\omega} \quad (23)$$

yields other convergent, accurate schemes (see, e.g., Winckelmans and Leonard [44]). The reason the direct scheme is here retained is that it behaves better than the other schemes based on Eq. (23) with respect to the divergence problem (Cottet [5], Cottet and Koumoutsakos [7]). By taking the divergence of Eq. (1), one finds that

$$\frac{D}{Dt} (\nabla \cdot \tilde{\boldsymbol{\omega}}) = \nu \nabla^2 (\nabla \cdot \tilde{\boldsymbol{\omega}}). \quad (24)$$

The direct scheme thus basically diffuses $\nabla \cdot \tilde{\boldsymbol{\omega}}$ (Cottet [5], Cottet and Koumoutsakos [7]).

The right-hand sides of Eqs. (21) and (22) are here computed using a parallel version of the fast multipole algorithm that has an operation count of $\mathcal{O}(N \log(N))$, and with active error control based on accurate error bounds (Barnes and Hut [2], Greengard and Rohklin [11], Salmon and Warren [40], Salmon *et al.* [41], Winckelmans *et al.* [45–47]).

3.2. Diffusion

The treatment of viscous diffusion is based on the technique of PSE (Degond and Mas-Gallic [9]). In this algorithm, the Laplacian operator ∇^2 is approximated by an integral operator,

$$\nabla^2 \omega(\mathbf{x}) \approx \frac{2}{\sigma^2} \int \eta_\sigma(\mathbf{x} - \mathbf{y}) (\omega(\mathbf{y}) - \omega(\mathbf{x})) d\mathbf{y}, \quad (25)$$

with $\eta_\sigma(\mathbf{x}) = \eta(|\mathbf{x}|/\sigma)/\sigma^3$ and $\eta(s) = -\frac{1}{s} \frac{d}{ds} \zeta(s)$. The Gaussian smoothing is such that $\eta_\sigma = \zeta_\sigma$. The integral operator in Eq. (25) is discretized using the particles, and the evolution equation for the particle strengths becomes

$$\left. \frac{d\alpha_i}{dt} \right|_{\text{PSE}} = \frac{2\nu}{\sigma^2} \sum_{j=1}^N (V_i \alpha_j - V_j \alpha_i) \eta_\sigma(\mathbf{x}_i - \mathbf{x}_j) \simeq \frac{2\nu}{\sigma^2} \sum_{j \in \mathcal{P}_i} (V_i \alpha_j - V_j \alpha_i) \eta_\sigma(\mathbf{x}_i - \mathbf{x}_j). \quad (26)$$

In practice, the right-hand side of Eq. (26) does not involve a contribution from all particles, as the rapid decrease of η_σ means that only the particles close to particle i contribute significantly to $d\alpha_i/dt$. The subset of such particles is denoted \mathcal{P}_i . If the Gaussian smoothing is used, \mathcal{P}_i consists, typically, of the particles less than 5σ from \mathbf{x}_i . With the fast multipole method, the velocity and velocity gradient induced by the particles in \mathcal{P}_i are always evaluated directly. Thus, as the exponential is already computed, the additional PSE cost is truly marginal. When σ is not the same for all particles, Eq. (26) is replaced by

$$\begin{aligned} \left. \frac{d\alpha_i}{dt} \right|_{\text{PSE}} &= 2\nu \sum_{j=1}^N \frac{1}{\sigma_{ij}^2} (V_i \alpha_j - V_j \alpha_i) \eta_{ij}(\mathbf{x}_i - \mathbf{x}_j) \\ &\simeq 2\nu \sum_{j \in \mathcal{P}_i} \frac{1}{\sigma_{ij}^2} (V_i \alpha_j - V_j \alpha_i) \eta_{ij}(\mathbf{x}_i - \mathbf{x}_j), \end{aligned} \quad (27)$$

with $\eta_{ij}(\mathbf{x}_i - \mathbf{x}_j) = \eta(|\mathbf{x}_i - \mathbf{x}_j|/\sigma_{ij})/\sigma_{ij}^3$. As for the original PSE, this symmetrized version is still conservative: $\frac{d}{dt}(\sum_{i=1}^N \alpha_i) = 0$. It is also still second-order accurate provided σ varies smoothly in space (Ploumhans and Winkelmanns [35, 36]). An alternative approach is to do the PSE in a mapped domain (Cottet *et al.* [6, 8], Ould Salihi [32], Cottet and Koumoutsakos [7]).

In the presence of solid boundaries, the PSE is further modified: When computing the PSE for particles close to the boundary, image particles are used. This technique was already explained and validated by Ploumhans and Winkelmanns [35, 36] for the 2-D case, and by Ploumhans *et al.* [34] for the 3-D case. In the 3-D case, the use of images allows elegant enforcement of the Dirichlet boundary condition on ω_n (Cottet, private communication, 1997). The computation of the PSE for particle i involves two subsets of particles: \mathcal{P}_i (the subset of particles *close enough* to \mathbf{x}_i) and \mathcal{P}'_i (the set of the images of the particles in \mathcal{P}_i). If the particle i is such that \mathbf{x}_i is more than d_s (typically 5σ for the Gaussian smoothing) from the body surface, S , images have no effect on $d\alpha_i/dt$; so \mathcal{P}'_i is empty. If \mathbf{x}_i is closer than d_s from S , each particle in \mathcal{P}_i has an image particle in \mathcal{P}'_i . If \mathbf{x}_j is the position of a particle in \mathcal{P}_i , \mathbf{x}'_j represents the position of its image. This position is computed using symmetry, the plane of symmetry being the plane tangent to S and closest to \mathbf{x}_i (see Fig. 1). The volume (V'_j) and smoothing parameter (σ'_j) of an image particle are taken equal to those of the

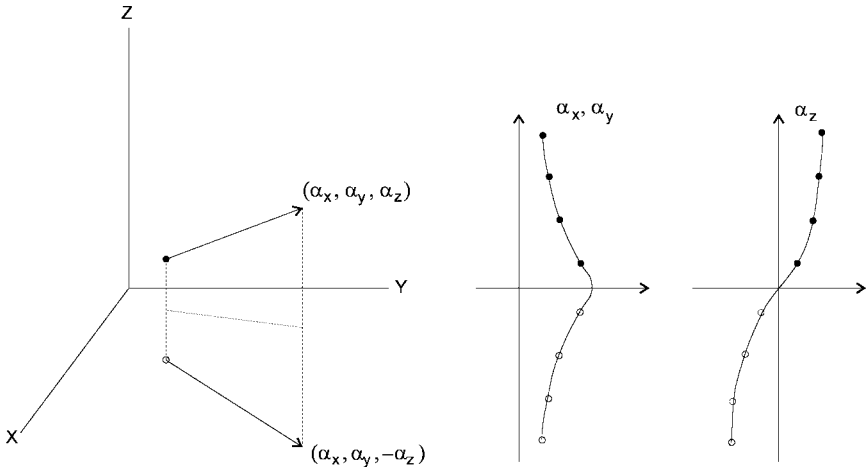


FIG. 1. Use of PSE images in 3-D. The tangent components have a symmetric image (α_x, α_y) ; the normal component has an antisymmetric image (α_z) .

original particle. The two components of the strength (α'_j) parallel to the tangential plane, T , are taken equal to those of α_j . The normal component is taken with the opposite sign (see Fig. 1).

The use of image particles guarantees that there is no spurious flux of the components of vorticity parallel to the wall during the PSE. It also ensures that the normal vorticity remains zero during the PSE. It can be shown (Cottet, private communication, 1997; Ploumhans *et al.* [34], Cottet and Koumoutsakos [7]), for the planar geometry, that if $\omega_n = 0$ and if $\nabla \cdot \omega = 0$, the enforcement of the Neumann boundary condition on the tangential components of ω (using the algorithm presented in Section 3.3 and 3.4) does not introduce vorticity divergence near the wall.

The convergence of the PSE in the presence of solid boundaries was studied by Mas-Gallic [27], who showed that in 2-D, with a uniform resolution and with a planar boundary, the image-modified PSE is first-order accurate. This proof was later extended to curved boundaries by Benhaddouch [4]. This last proof also shows that the accuracy of the image-modified PSE decreases as the curvature of the boundary increases. This calls for alternative approaches when one deals with bodies involving sharp edges. One possibility is to use the recent developments of Eldredge *et al.* [10], who developed “one-sided” approximations of derivative operators, which only gather information where it is available. This could also be applied for slender bodies.

3.3. Computation of the Vortex Sheet

The vector-valued vortex sheet, $\Delta\gamma$, necessary on the body surface to cancel the slip velocity, $\Delta\mathbf{U}_{\text{slip}}$, is the solution of the Fredholm boundary integral equation of the second kind,

$$\frac{1}{2} \Delta\gamma(\mathbf{x}) \times \mathbf{n} + \frac{1}{4\pi} \int_S \frac{1}{|\mathbf{x} - \mathbf{x}'|^3} \cdot (\mathbf{x} - \mathbf{x}') \times \Delta\gamma(\mathbf{x}') d\mathbf{x}' = \Delta\mathbf{U}_{\text{slip}}, \quad (28)$$

where \mathbf{n} points inside the fluid. The left-hand side of Eq. (28) is the opposite of the velocity induced by the vortex sheet, at a point located on the surface.

The vector sheet, $\Delta\gamma$, is parallel to the body surface (hence only two components need to be determined). Under the assumption that ω and ψ are divergence free, it is easily seen that cancelling the two tangential components of the velocity at the wall automatically guarantees that the normal velocity is also zero. One first considers the following identity:

$$\int_{\text{body}} \psi \cdot (\nabla \times (\nabla \times \psi)) dV = \int_{\text{body}} |\nabla \times \psi|^2 dV - \int_S \psi \cdot ((\nabla \times \psi) \times \mathbf{n}) dS. \quad (29)$$

Since $\mathbf{u} = \nabla \times \psi$ and $\omega = \nabla \times \mathbf{u} = \nabla \times (\nabla \times \psi)$, Eq. (29) can be rewritten as

$$\int_{\text{body}} \psi \cdot \omega dV = \int_{\text{body}} |\mathbf{u}|^2 dV - \int_S \psi \cdot (\mathbf{u} \times \mathbf{n}) dS. \quad (30)$$

For a nonrotating body, $\omega = \mathbf{0}$ everywhere inside the body, so the left-hand side of Eq. (30) vanishes. If $\mathbf{u} \times \mathbf{n}$, the tangential velocity, is also zero at the wall, Eq. (30) becomes

$$\int_{\text{body}} |\mathbf{u}|^2 dV = 0, \quad (31)$$

which means that the velocity is zero everywhere inside the body (and thus that $\mathbf{u} \cdot \mathbf{n}$ vanishes at the wall).

To solve Eq. (28), the body surface is discretized using M boundary elements (i.e., “vortex sheet panels”), each of size $O(h)$ (with h the typical distance between particles in the vicinity of the body) and each of uniform strength. For each computational panel on the body, the slip velocity underneath that panel is taken as the average, over the panel, of the slip velocity induced by the free stream and by all vortex particles which, for this step only, are considered point vortices (to ensure that all the vorticity is indeed outside of the body). The average velocity is evaluated numerically, by integrating with some appropriate numerical quadrature (e.g., Hammer quadrature for triangular panels) the slip velocity obtained from the fast algorithm. Once the panel-averaged slip velocity, $\Delta\bar{\mathbf{U}}_{\text{slip}}$, has been evaluated for all panels, computing the panel strengths to cancel it amounts to solving a linear system. This is because, in addition to inducing a uniform tangential velocity underneath themselves (equal to $\mathbf{n} \times \Delta\gamma/2$), the panels also induce a tangential velocity on one another, as expressed by Eq. (28). Notice that the tangential velocity induced by one panel on another is also averaged over that panel, using the same numerical quadrature as above.

The solution of the linear system is obtained iteratively, using an underrelaxed Jacobi. Each iteration requires a matrix vector multiply; thus there is an $O(M^2)$ computational cost if classical methods are used. Furthermore, for large values of M , storing all M^2 matrix elements is completely impractical. The computational cost is here drastically reduced by using the multipole expansion representation of the panels to efficiently evaluate the matrix vector product. This leads to a computational cost that is $O(M \log M)$ per iteration. Such a fast solver (implemented by Winckelmans *et al.* [45–47]) has been used for all the simulations presented in this paper. The iterative procedure is stopped when the criterion

$$\sqrt{\sum_P |\Delta\bar{\mathbf{U}}_{\text{slip}}^P + \bar{\mathbf{u}}_{\Delta\gamma}^2|^2 \cdot S^P} < \epsilon_p \sqrt{\sum_P |\Delta\bar{\mathbf{U}}_{\text{slip}}^P|^2 S^P}, \quad (32)$$

where S_P is the surface of panel P , $\Delta\bar{\mathbf{U}}_{\text{slip}}^P$ is the slip velocity averaged over panel P , and $\bar{\mathbf{u}}_{\Delta\gamma}^P$ is the vortex sheet induced velocity (from all vortex panels) averaged over panel P ,

is satisfied. A typical value for ϵ_p is 10^{-4} . As one can use, as first guess, the vortex sheet strength at the previous time step (except at $t = 0$), the iterative method converges fast: For the simulations presented in Section 5, seven iterations were typically required. Because they are many more vortex particles than vortex panels, the cost of solving for the vortex sheet strength is much less than the rest (10–15% when the wake is developed).

3.4. Vortex Sheet Diffusion

The total flux to be emitted into the flow for the other substep of the diffusion process is given by

$$\nu \frac{\partial \omega}{\partial n} = \frac{\Delta \gamma}{\Delta t}, \quad (33)$$

with \mathbf{n} pointing toward the fluid. This flux must be emitted during a time Δt . In effect, the vortex sheet $\Delta \gamma$ must be distributed to neighbor particles by discretizing the Green's integral for the inhomogeneous Neumann problem corresponding to the diffusion equation (see Koumoutsakos *et al.* [17] for a simple scheme in 2-D). Leonard *et al.* [21], Ploumhans *et al.* [34], and Ploumhans and Winckelmans [35, 36] have proposed a more accurate scheme. The difference between this new scheme and the previous one, together with a numerical test showing its enhanced accuracy, was detailed in [35, 36]. The extension of this scheme to 3-D is straightforward (Ploumhans *et al.* [34]). Consider a rectangular panel of uniform strength $\Delta \gamma$ and size $b \times f$, located on the XY plane, and diffusing toward the positive Z direction, as shown in Fig. 2. A particle located at (x_i, y_i, z_i) , ($z_i > 0$), receives, from that

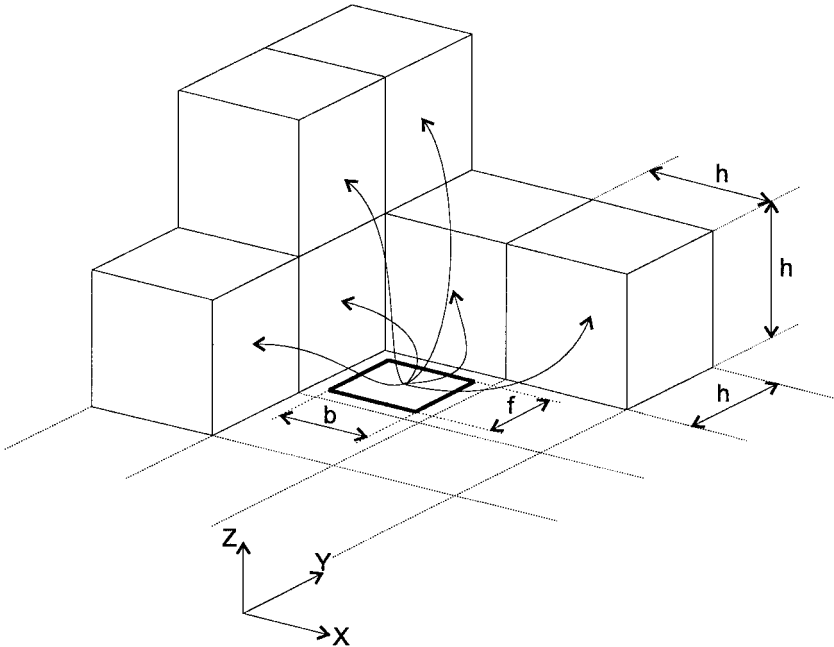


FIG. 2. Panel to particles diffusion in 3-D.

panel, an amount of “vorticity \times volume” given by

$$\Delta\alpha_i = \int_0^{\Delta t} \frac{d\alpha_i}{dt} dt, \quad (34)$$

with

$$\frac{d\alpha_i}{dt} = \int_{x_i-h_i/2}^{x_i+h_i/2} \int_{y_i-h_i/2}^{y_i+h_i/2} \int_{z_i-h_i/2}^{z_i+h_i/2} \frac{d\omega}{dt} dx dy dz, \quad (35)$$

where $d\omega/dt$, the rate of change of the vorticity due to the panel, is equal to

$$\frac{d\omega}{dt} = \frac{\Delta\gamma}{\Delta t} \frac{1}{2\sqrt{\pi}} \frac{1}{\sqrt{4vt}} \exp\left(-\frac{z^2}{4vt}\right) [\text{erfc}(s)]_{(x-b/2)/\sqrt{4vt}}^{(x+b/2)/\sqrt{4vt}} [\text{erfc}(s)]_{(y-f/2)/\sqrt{4vt}}^{(y+f/2)/\sqrt{4vt}}. \quad (36)$$

Equation (35) is then integrated exactly, giving

$$\begin{aligned} \frac{d\alpha_i}{dt} &= \frac{\Delta\gamma}{\Delta t} \left([\text{ierfc}(u)]_{(z_i-h_{i,l}/2)/\sqrt{4vt}}^{(z_i+h_{i,l}/2)/\sqrt{4vt}} \right) \\ &\times \left(\sqrt{4vt} \frac{1}{2} \left([\text{ierfc}(u)]_{(x_i-h_i/2-b/2)/\sqrt{4vt}}^{(x_i+h_i/2-b/2)/\sqrt{4vt}} - [\text{ierfc}(u)]_{(x_i-h_i/2+b/2)/\sqrt{4vt}}^{(x_i+h_i/2+b/2)/\sqrt{4vt}} \right) \right) \\ &\times \left(\sqrt{4vt} \frac{1}{2} \left([\text{ierfc}(u)]_{(y_i-h_i/2-f/2)/\sqrt{4vt}}^{(y_i+h_i/2-f/2)/\sqrt{4vt}} - [\text{ierfc}(u)]_{(y_i-h_i/2+f/2)/\sqrt{4vt}}^{(y_i+h_i/2+f/2)/\sqrt{4vt}} \right) \right), \quad (37) \end{aligned}$$

where $\text{ierfc}(s) = \int_s^\infty \text{erfc}(v) dv = \frac{1}{\sqrt{\pi}} \exp(-s^2) - s \text{erfc}(s)$. Notice that $h_{i,l}/2 = z_i$ if $0 \leq z_i < h_i$ and $h_{i,l}/2 = h_i/2$ otherwise. This allows for particles in the “first layer” to be closer to or further away from the XY plane than $h_i/2$, and it ensures that the scheme remains conservative in such cases. The time integral in Eq. (34) is evaluated numerically using a Gauss quadrature (four points). Equation (37) is exact for a rectangle panel of size $b \times f$. To still use Eq. (37) when the discretization of the vortex sheet is done using triangular panels, each triangular panel is considered, for the diffusion step, as a square (centered at the triangle centroid, and of surface equal to that of the triangle).

If particles are on a regular lattice aligned with the panel (as shown in Fig. 2), Eq. (37) leads to a conservative scheme. In practice, however, the spatial distribution of the particles is not well aligned with the vortex panels: The proposed scheme is then not exactly conservative. To enforce conservation, the following correction is made: Instead of using directly $\Delta\alpha_i$ given by Eq. (34) one uses

$$\Delta\alpha_{i,\text{conserv}} = \Delta\alpha_i + \frac{|\Delta\alpha_i|^2}{\sum_j |\Delta\alpha_j|^2} \left(S \Delta\gamma - \sum_j \Delta\alpha_j \right), \quad (38)$$

where j runs over all particles concerned by the panel. This scheme minimizes $\sum_i |\Delta\alpha_i - \Delta\alpha_{i,\text{conserv}}|^2 / |\Delta\alpha_i|^2$ with the constraint that $(S \Delta\gamma) - (\sum_i \Delta\alpha_{i,\text{conserv}}) = 0$.

For diffusion with the above scheme to work properly, the spatial distribution of the particles must remain fairly uniform. This is one reason why particle redistribution is needed every 5–10 time steps. Of course, as in vortex methods without solid boundaries, it is also needed to minimize the PSE, convection, and stretching errors.

3.5. Particle Redistribution

In accurate particle methods for direct numerical simulation (DNS) of viscous flows, one needs to maintain the condition that particle cores overlap at all times. This is a required criterion for the convergence of the vortex method (Beale [3], Hald [12]) and calls for a particle redistribution scheme. It consists of replacing the distorted set of vortex particles with a new set where the particles are, again, located on an $h \times h \times h$ lattice. If σ is not the same for each particle, the redistribution is performed in a mapped domain (see Section 3.6) in which particles are located on a $1 \times 1 \times 1$ mapped lattice after redistribution. The volume $V_i = h_i^3$ of each particle in the new set is determined by the mapping (see Section 3.6). The smoothing parameter is taken as $\sigma_i = \beta h_i$, with β the core overlapping parameter (typically, $\beta = 1$ for the Gaussian as defined in Eq. (7)). For particles close to the body, the surface is “corrected” in order to take into account the fact that part of the volume V_i associated to particle i is “inside” the body.

The redistribution is performed in such a way that the moments of order zero, one, and two of the vorticity field are conserved. This is required by the physics, as these moments correspond, respectively, to the total vorticity, the linear impulse, and the angular impulse. On top of the physical reason to conserve these moments, there is also a mathematical one: Performing an analysis of the vorticity field in the Fourier space, Koumoutsakos [16, 20] showed that the difference between the vorticity field computed (using Eq. (5)) from the distorted set of particles, and from the redistributed one, decreases as the number of moments that are conserved increases.

The technique used to perform such a redistribution in the presence of solid boundaries that intersect the redistribution lattice in an arbitrary way, has already been described for the 2-D case (Ploumhans *et al.* [34], Ploumhans and Winckelmans [35, 36]). Since the extension to 3-D is straightforward, it is not detailed here.

When performing a redistribution, one guarantees a minimum distance, d_{halo} , between a new particle and the body surface (typically, $d_{\text{halo}} = h/4$, where h is the distance between the particles close to the body surface). Numerical tests have indeed shown that this helps keep the particles outside the body. If a particle comes inside, action has to be taken (for example by relocating the particle outside); otherwise the particle will induce a very spurious slip velocity (and thus a very spurious vortex sheet), something that usually leads to a fast numerical blowup. However, relocating the particles breaks the vortex lines and, thus, worsens the sensivity of the method to the divergence problem. Numerical experiments have also shown the effect to be cumulative: If particles cross the boundary at one time step and nothing is done, more particles will cross the boundary at the next time step. Therefore, if particles cross the boundary, they are relocated outside, and an “emergency” redistribution is performed at the next time step. Numerical tests have shown this procedure to be acceptable, as long as it remains an occasional event. By occasional, we mean that it can only occur during intense acceleration phases (such as an impulsive start). During only one of the three simulations presented in Section 5 did a particle cross the body: One particle crossed the body, just after the body was impulsively started. Recent tests have shown that using a smaller time step during the acceleration phases eliminates this phenomenon (Daeninck, private communication, 2001).

Notice that the 3-D situation is significantly different from the 2-D situation, where it was better to let particles come inside the body and correct their position than to use a “halo.” This was shown, in 2-D, by Ploumhans and Winckelmans [35, 36], who tested several techniques to compute the flow past an impulsively started cylinder, using an $h \times h$

redistribution lattice. Simulations were performed at $Re = U_\infty D/\nu = 550$ and 3000, and the results were compared with an analytical reference solution (Bar-Lev and Yang [1]) at short times, and with a numerical reference solution computed using a body-fitted redistribution lattice (similar to the one used by Koumoutsakos and Leonard [18]) at long times. Although the techniques using $d_{\text{halo}} = 0$ led to more particles crossing the boundary, they also led to (slightly) more accurate results than those using $d_{\text{halo}} = h/4$. Let us also mention that (a) the difference with the other techniques was marginal, even just after the impulsive start [35, 36], and (b) since d_{halo} is proportional to h , it goes to zero as h vanishes, so that using a halo does not prevent the method from converging (this, too, was tested in 2-D).

A difficulty that occurs in dealing with the redistribution is to decide when to apply it. No clear criterion exists. On one hand, to best preserve particle overlap, it is better to redistribute frequently. On the other hand, higher order redistribution introduces a hyper-viscous type of dissipation (Koumoutsakos [20]), so that one does not want to apply it too frequently, to keep the redistribution-induced dissipation much smaller than the viscosity-induced one. Koumoutsakos [20] tested the influence of the redistribution frequency on an inviscid flow, the axisymmetrization of an elliptical vortex, and found no noticeable difference between the numerical dissipation obtained by redistributing every 9 steps and every 17 steps. Koumoutsakos and Shiels [19] also tested the influence of the redistribution on the viscous flow past an impulsively started flat plate. Redistributing every 6, 12, or 24 steps led to the same level of accuracy of the drag coefficient as a function of time, but the last redistribution frequency produced noisier results. In most of their simulations, they used a redistribution criterion based on the conservation of global quantities of the flow but always redistributed at least once every 10 steps. On the other hand, Cottet *et al.* [6] computed the 3-D viscous interaction of a vortex ring with a plane and performed a redistribution every time step. Even in this extreme case, they reported that the redistribution “produces no discernable extra dissipation.” However, they mention that in turbulent flows the redistribution could act at a subgrid level.

In Ploumhans and Winckelmans [35, 36], 2-D simulations of the flow past a cylinder were performed using a redistribution lattice that crosses the boundary arbitrarily. The redistribution was performed every five time steps, and comparisons with a reference solution and a convergence analysis confirmed that this value produced accurate results. As the vortex method presented in this paper is a direct 3-D extension of the 2-D method presented in [35, 36], we keep using the same criterion and redistribute every five time steps.

3.6. Redistribution with Mapping of the Physical Domain

In external flows, the vorticity is located in the boundary layer and in the wake, with the magnitude of the vorticity decreasing as one goes away from the body. It is thus more efficient to have high resolution near the body and coarser resolution in the wake. To achieve this, the physical domain, with spatially varying resolution, is mapped onto a regular indicial lattice (i, j, k) . This approach has been used previously to perform 2-D simulations (Cottet *et al.* [6, 8], Ould Salihi [32], Cottet and Koumoutsakos [7], Ploumhans and Winckelmans [35, 36]). It is here extended to the 3-D case. The mapping used in this paper is given by

$$\begin{cases} x = x_0 + r(i) \cos \theta(j) \cos \phi(k) \\ y = y_0 + r(i) \sin \theta(j) \cos \phi(k) \\ z = z_0 + r(i) \cos \theta(j) \sin \phi(k), \end{cases} \quad (39)$$

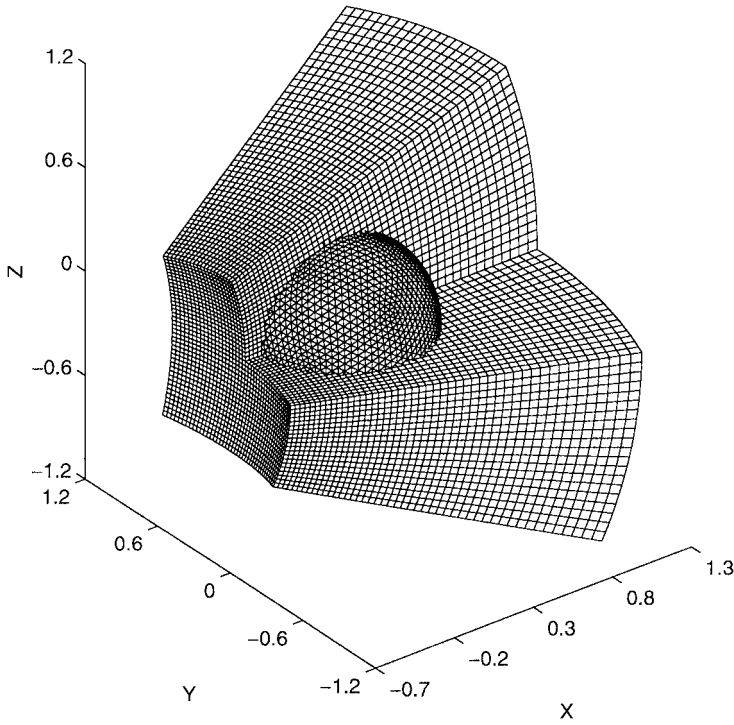


FIG. 3. Redistribution mapping with $m = 350$, $x_0/D = -2$, $y_0/D = z_0/D = 0$, and $R_0/D = 0.5$, and sphere discretization with $M = 5120$ triangles. At $Re = 300$, a value of $m = 700$ is used, together with $M = 20,480$ triangles. At $Re = 500$, $m = 950$ and $M = 20480$. At $Re = 1000$, $m = 1350$ and $M = 81,920$.

with $\theta(j) = 2(\pi/m)j$, $\phi(k) = (2\pi/m)k$, $-m/2 \leq j, k \leq m/2$, and $r(i) = R_0 f(i)$. The function $f(i)$ is chosen as in 2-D:

$$f(i) = \exp\left(\frac{2\pi}{m}i\right). \quad (40)$$

Figure 3 shows an example of the redistribution mapping. The Jacobian of the mapping, J , is equal to

$$J = \left(\frac{2\pi}{m}\right)^3 r^3(i) \cos\left(\frac{2\pi}{m}j\right) \cos\left(\frac{2\pi}{m}k\right). \quad (41)$$

It is seen to be zero for $j = \pm m/4$ and $k = \pm m/4$. In practice, this is not a problem, because the parameters of the mapping are chosen such that particles remain “far” from these singularities. There is another reason to use moderate values of j/m and k/m : the desire that the volume associated with each particle (which is a $1 \times 1 \times 1$ cube in the mapped domain) be as close as possible to a cube in the physical domain. Indeed, one would like that if $di = dj = dk$, then

$$\left|\frac{\partial \mathbf{x}}{\partial i}\right| di = \left|\frac{\partial \mathbf{x}}{\partial j}\right| dj = \left|\frac{\partial \mathbf{x}}{\partial k}\right| dk. \quad (42)$$

In practice, one considers

$$A_R^1 = \left| \frac{\partial \mathbf{x}}{\partial j} \right| \left/ \left| \frac{\partial \mathbf{x}}{\partial i} \right| \right., \quad (43)$$

$$A_R^2 = \left| \frac{\partial \mathbf{x}}{\partial k} \right| \left/ \left| \frac{\partial \mathbf{x}}{\partial i} \right| \right., \quad (44)$$

which is a measure of the lattice anisotropy in the physical domain, with

$$\left| \frac{\partial \mathbf{x}}{\partial j} \right| \left/ \left| \frac{\partial \mathbf{x}}{\partial i} \right| \right. = \sqrt{\frac{\cos^2 \phi + \sin^2 \theta \sin^2 \phi}{\cos^2 \phi + \cos^2 \theta \sin^2 \phi}}, \quad (45)$$

$$\left| \frac{\partial \mathbf{x}}{\partial k} \right| \left/ \left| \frac{\partial \mathbf{x}}{\partial i} \right| \right. = \sqrt{\frac{\cos^2 \theta + \sin^2 \theta \sin^2 \phi}{\cos^2 \phi + \cos^2 \theta \sin^2 \phi}}. \quad (46)$$

If θ and ϕ are both less than 25 deg, one has

$$0.91 \leq A_R^1 \leq 1 \quad \text{and} \quad 0.91 \leq A_R^2 \leq 1. \quad (47)$$

This is the case for all the simulations presented hereafter.

After each redistribution, new particles in the mapped domain have position $(i + 1/2, j + 1/2, k + 1/2)$ and the corresponding positions obtained from Eqs. (39) and (40) in the physical domain. The volume of fluid associated with the particle is computed:

$$\begin{aligned} V = h^3 &= \iiint J \, di \, dj \, dk \\ &= \int_i^{i+1} \int_j^{j+1} \int_k^{k+1} \left(\frac{2\pi}{m} R_0 \right)^3 \exp\left(\frac{6\pi}{m} i\right) di \cos\left(\frac{2\pi}{m} j\right) dj \cos\left(\frac{2\pi}{m} k\right) dk \\ &= \frac{R_0^3}{3} \left(\exp\left(\frac{6\pi}{m}(i+1)\right) - \exp\left(\frac{6\pi}{m} i\right) \right) \left(\sin\left(\frac{2\pi}{m}(j+1)\right) \right. \\ &\quad \left. - \sin\left(\frac{2\pi}{m} j\right) \right) \cdot \left(\sin\left(\frac{2\pi}{m}(k+1)\right) - \sin\left(\frac{2\pi}{m} k\right) \right) \\ &= \frac{8}{3} R_0^3 \exp\left(\frac{6\pi}{m}(i+1/2)\right) \sinh\left(\frac{3\pi}{m}\right) \cos\left(\frac{2\pi}{m}(j+1/2)\right) \\ &\quad \times \sin\left(\frac{\pi}{m}\right) \cos\left(\frac{2\pi}{m}(k+1/2)\right) \sin\left(\frac{\pi}{m}\right). \end{aligned} \quad (48)$$

For small values of π/m , this reduces to

$$V = h^3 \simeq \left(\frac{2\pi}{m} R_0 \exp\left(\frac{2\pi}{m}(i+1/2)\right) \right)^3 \cdot \cos\left(\frac{2\pi}{m}(j+1/2)\right) \cdot \cos\left(\frac{2\pi}{m}(k+1/2)\right). \quad (49)$$

The smoothing parameter, σ , associated with the particle is taken as $\sigma = \beta h$, where β is the core overlapping parameter (for the Gaussian, $\beta = 1$ is used). The use of this mapping produces a σ that varies smoothly in space: Eq. (27) can thus be used safely, preserving the second-order accuracy of the PSE.

4. FORCE EVALUATION IN VORTEX METHODS

In vortex methods, the classical technique to evaluate the force \mathbf{F} acting on a body is to compute the time derivative of the linear impulse,

$$\frac{\mathbf{F}}{\rho} = -\frac{d\mathbf{I}}{dt}, \quad (50)$$

where ρ is the density, and \mathbf{I} is given by

$$\mathbf{I} = \frac{1}{\mathcal{N}-1} \int_V \mathbf{x} \times \boldsymbol{\omega} dV, \quad (51)$$

with \mathcal{N} the dimension of the space ($\mathcal{N} = 3$ in 3-D, $\mathcal{N} = 2$ in 2-D), and V the volume occupied by the fluid. This method (referred to hereafter as method A) is very robust and has an almost zero computational cost, as it is implemented as a sum running over all particles. However, when performing simulations with nonuniform resolution (as is absolutely necessary for long time simulations; see Section 5), the far wake could become underresolved, thereby degrading the accuracy of \mathbf{I} and \mathbf{F} . It is thus desirable to also be able to evaluate the force by a local method instead of a global one.

An alternative to the global method, Eqs. (50) and (51), is to perform a momentum balance on a control volume (CV) that encloses the body (this second approach is referred to hereafter as method B). Such an approach was developed by Noca *et al.* [30, 31]. Consider a control volume V_{CV} , with outer surface S_{CV} , and inner surface S , the body surface. The force acting on the body can be expressed as [30, 31]

$$\begin{aligned} \frac{\mathbf{F}}{\rho} = & -\frac{1}{\mathcal{N}-1} \frac{d}{dt} \int_{V_{CV}} \mathbf{x} \times \boldsymbol{\omega} dV + \int_{S_{CV}} \left(\frac{1}{2} (\mathbf{u} \cdot \mathbf{u}) \mathbf{n} - (\mathbf{n} \cdot \mathbf{u}) \mathbf{u} \right) dS \\ & - \frac{1}{\mathcal{N}-1} \int_{S_{CV}} (\mathbf{n} \cdot \mathbf{u}) (\mathbf{x} \times \boldsymbol{\omega}) dS + \frac{1}{\mathcal{N}-1} \int_{S_{CV}} (\mathbf{n} \cdot \boldsymbol{\omega}) (\mathbf{x} \times \mathbf{u}) dS \\ & + \frac{1}{\mathcal{N}-1} \int_{S_{CV}} \mathbf{x} \times (\mathbf{n} \times \nabla \cdot \mathbf{T}) dS + \int_{S_{CV}} \mathbf{n} \cdot \mathbf{T} dS \\ & + \frac{1}{\mathcal{N}-1} \frac{d}{dt} \int_S \mathbf{x} \times (\mathbf{n} \times \mathbf{u}) dS - \int_S \mathbf{n} \cdot \mathbf{u} dS, \end{aligned} \quad (52)$$

with $\mathbf{T} = \nu(\nabla \mathbf{u} + (\nabla \mathbf{u})^T)$. If the velocity vanishes at the wall, the integrals on S cancel. In that case, Eq. (52) does not require information at the boundary, and the CV can be chosen so as to enclose only a well-resolved region of the flow. The volume integral in Eq. (52) is the same as the one appearing in Eq. (51). Method B is best viewed as method A applied to the part of the flow inside S_{CV} , complemented by a surface integral that accounts for the momentum flux through S_{CV} . If the CV is extended to infinity, one recovers Eq. (50). The surface integrals in Eq. (52) are evaluated using the regularized velocity field and its derivatives. The evaluation of the volume integral in Eq. (52) is difficult: One could decide to use either singular particles (for which the integral becomes a sum running over all particles inside V_{CV} , but then the regularization of the particles is not the same as for the surface integrals) or regularized particles (for which the volume integral is difficult to evaluate

accurately, because particles close to S_{CV} have vorticity contribution partly outside and partly inside the CV). Neither solution is satisfactory. It is more advantageous to transform the volume integral into a surface integral, which can then be evaluated using the regularized fields

$$\int_{V_{CV}} \mathbf{x} \times \boldsymbol{\omega} dV = \int_{S_{CV}+S} ((\mathbf{u} \cdot \mathbf{x})\mathbf{n} - \mathbf{u}(\mathbf{x} \cdot \mathbf{n}) + (\mathcal{N} - 1)\mathbf{x}(\mathbf{u} \cdot \mathbf{n})) dS. \quad (53)$$

Note that the surface integral on S vanishes when $\mathbf{u} = \mathbf{0}$ at the wall (as for the flows considered in this paper). Method B then enables evaluating of the force acting on a body by performing only surface integrals. If several bodies are present, the force acting on each body can also be found: by using one CV enclosing each body.

5. FLOW PAST A SPHERE

The capabilities of the present method are illustrated on the flow past a sphere. This flow is considered because (a) it is a benchmark for bluff-body flows, and (b) it has been investigated numerically and experimentally by other authors.

The flow past a sphere exhibits different behaviors as the Reynolds number, $Re = U_\infty D / \nu$, is increased. As long as $Re < Re_1$, the flow remains steady and axisymmetric. Experimental investigations (Wu and Faeth [48], Magarvey and Bishop [26]), linear stability analysis (LSA) (Natarajan and Acrivos [29]), and numerical simulations (Tomboulides [42], Johnson [14], Johnson and Patel [15], Tomboulides and Orszag [43]) all agree that Re_1 is in the 210–212 range. If $Re > Re_1$, the flow remains steady but is not axisymmetric anymore. A second transition occurs at $Re = Re_2$, above which the flow becomes unsteady but still exhibits (a) time periodicity and (b) planar symmetry. Experiments by Magarvey and Bishop [25] and by Levi [24] predict a value for Re_2 in the 270–290 range. More recently, the experimental work of Ormières and Provansal [33] has narrowed the range to 275–285. The LSA study of Natarajan and Acrivos [29] predicts a value of $Re_2 = 277.5$. Numerical simulations by Tomboulides [42], and Tomboulides and Orszag [43], predict $270 < Re_2 < 285$; those by Johnson [14], and Johnson and Patel [15], predict $270 < Re_2 < 280$. A third transition appears at Re_3 , above which the time periodicity and planar symmetry are lost. The experiments of Sakamoto and Haniu [38, 39] predict that $Re_3 \approx 420$, while numerical investigations by Mittal [28] indicate a loss of planar symmetry and periodicity for a critical Reynolds number that lies in the 350–375 range. The numerical results of Tomboulides [42] and Tomboulides and Orszag [43] at $Re = 500$ indicate that periodicity and symmetry are indeed already lost. At even higher Reynolds numbers ($Re > 800$), it is seen experimentally that smaller scales appear. At these Reynolds number, a Kelvin–Helmholtz instability appears in the axisymmetric shear layer that results from the separation of the boundary layer.

We here performed numerical simulations at three Reynolds numbers, each corresponding to a different flow behavior: $Re = 300$, 500, and 1000.

5.1. $Re = 300$

The flow at $Re = 300$ is first considered, because it has been thoroughly analyzed numerically by Tomboulides [42], Johnson [14], Johnson and Patel [15], and Tomboulides and

Orszag [43]. Furthermore, as explained in the previous section, at this Reynolds number the flow attains a time periodic regime, making it practical and meaningful to compare mean drag and lift coefficients. The flow is here started impulsively, and a perturbation is applied to trigger the instability: Between $T \triangleq tU_\infty/D = 3$ and $T = 4$, the y component of the free-stream velocity is $U_{\infty,y} = \sin(\pi(T - 3))$.

The time step for the simulation is $\Delta T = 0.0125$. The parameters of the mapping, Eqs. (39) and (40), are $x_0/D = -2$, $y_0/D = z_0/D = 0$, $m = 700$, $R_0 = 0.5$. Redistribution is performed every five time steps. No particles have crossed the body surface during this simulation. If a new particle has $|\alpha| < 10^{-4}|\alpha|_{\max}$ and $Re_h = |\omega|h^2/\nu < Re_{h,\text{trsh}}$ (with $|\omega|h^2 \simeq |\alpha|/h$), it is deleted to avoid too high a growth rate for the number of particles. A value of $Re_{h,\text{trsh}} = 10^{-4}$ was used. The presence of seven layers of particles around the body is enforced after each redistribution. A halo is used with $d_{\text{halo}}/D = 4.5 \times 10^{-3}$. Gaussian particles are used with $\sigma/h = \beta = 1$. Equation (34) is integrated using four Gauss points. A four-point Hammer rule is used to compute the panel-averaged velocities (slip velocity and panel-induced velocity). The sphere is discretized using an icosahedron that is split recursively and blown on a sphere. At $Re = 300$, 20,480 triangular panels are used. Figure 3 shows the redistribution mapping together with the sphere discretization at a resolution twice coarser than what was used for $Re = 300$. The control volume used to compute the force with method B (see Section 4) is a sphere centered at $\mathbf{0}$, with diameter $D_{CV} = 2D$, and discretized by $M_{CV} = 20,480$ triangles. A parallel fast tree code is used (Winckelmans *et al.* [45–47]). The mean error estimate on the norm of the Biot–Savart velocity evaluated at the particles is $\sim 5.5 \times 10^{-3}U_\infty$. The number of particles goes from $\sim 141,000$ to $\sim 616,000$ (see Fig. 4), and the total run time is roughly 220 h on 32 processors of an HP V-Class system.

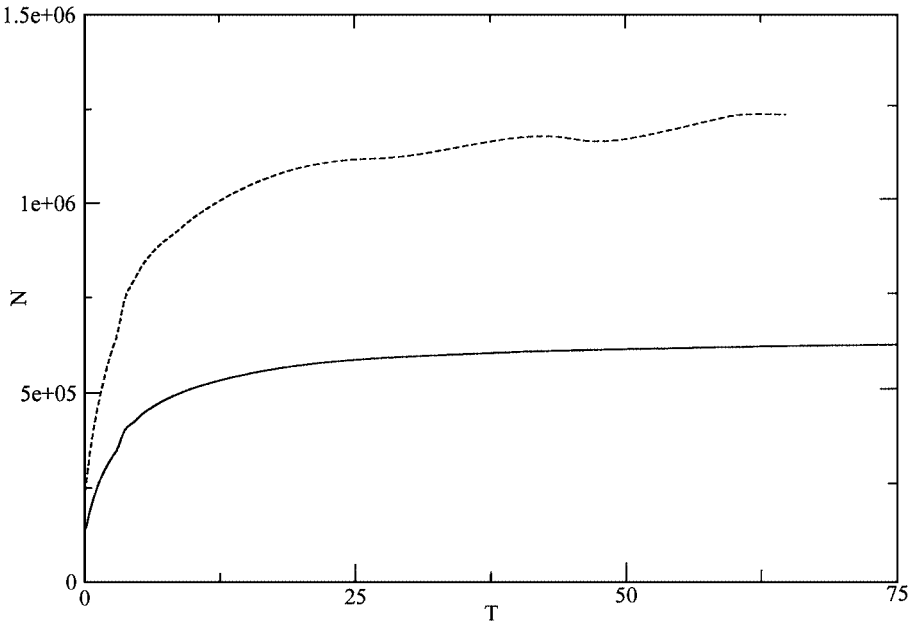


FIG. 4. Flow past a sphere. Number of particles as a function of time for $Re = 300$ (solid line) and $Re = 500$ (dashed line).

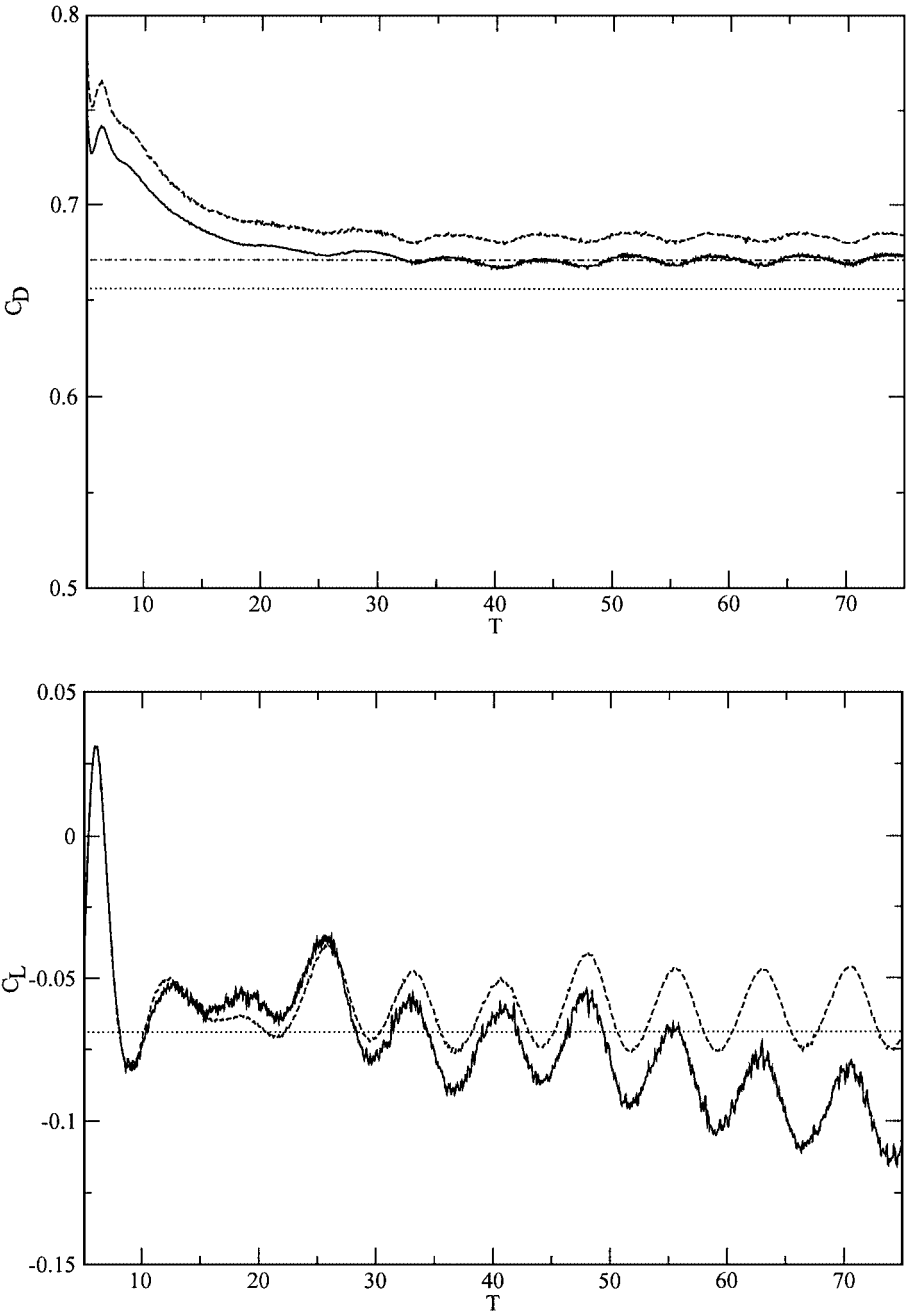


FIG. 5. C_D (top) and C_L (bottom) comparison for the flow past a sphere at $Re = 300$. Method A (solid), method B (dashed), and mean values of Tomboulides and Orszag (chain-dot) and of Johnson and Patel (dotted).

Figure 5 provides the force coefficients versus time, $C_D = F_x / ((\frac{1}{2}\rho U_\infty^2)(\pi D^2/4))$ and $C_L = F_y / ((\frac{1}{2}\rho U_\infty^2)(\pi D^2/4))$, computed using methods A and B (see Section 4). It is seen that after $T \simeq 30$, method A fails to predict a proper lift coefficient. The reason method A predicts a lift of ever increasing magnitude while predicting a drag that remains bounded can be understood by looking at the x and y components of the linear impulse \mathbf{I} . Using the

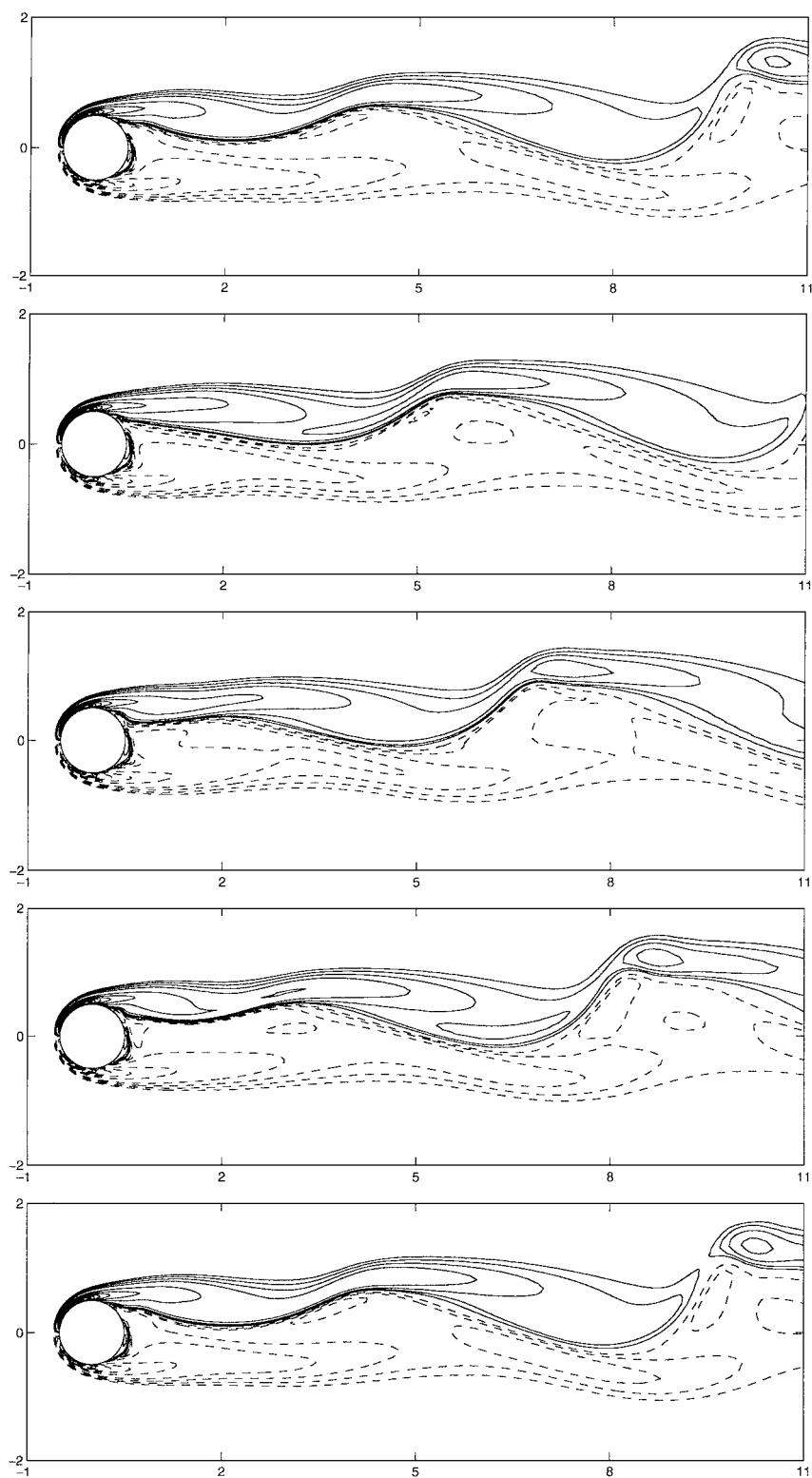


FIG. 6. Flow past a sphere at $Re = 300$. Contours of ω_z in the XY plane for every quarter period. Levels are by steps of 2, with additional contours at ± 0.5 , ± 0.25 , and ± 0.125 (zero level is skipped).

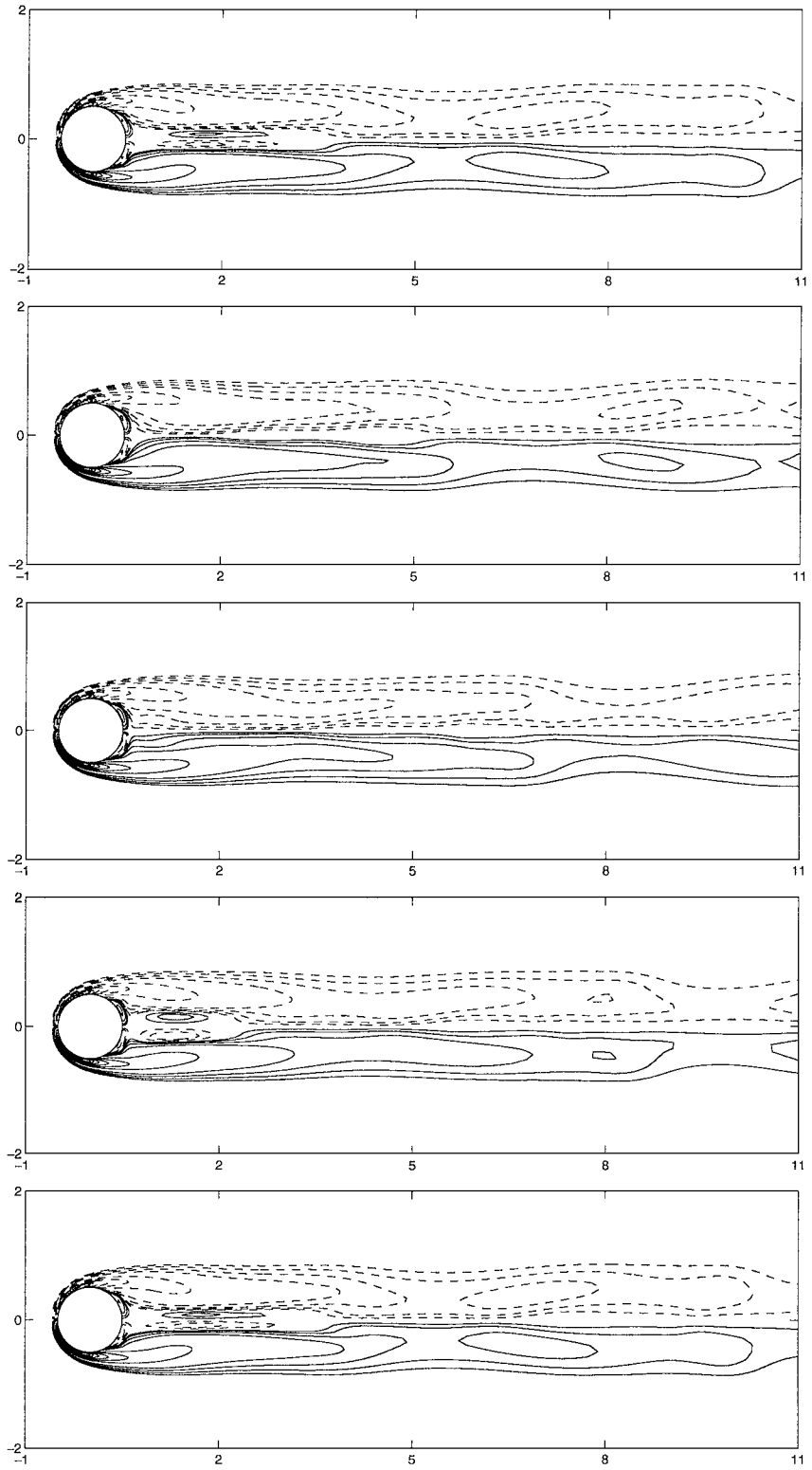


FIG. 7. Flow past a sphere at $Re = 300$. Contours of ω_y in the XZ plane for every quarter period. Levels are by steps of 2, with additional contours at ± 0.5 , ± 0.25 , and ± 0.125 (zero level is skipped).

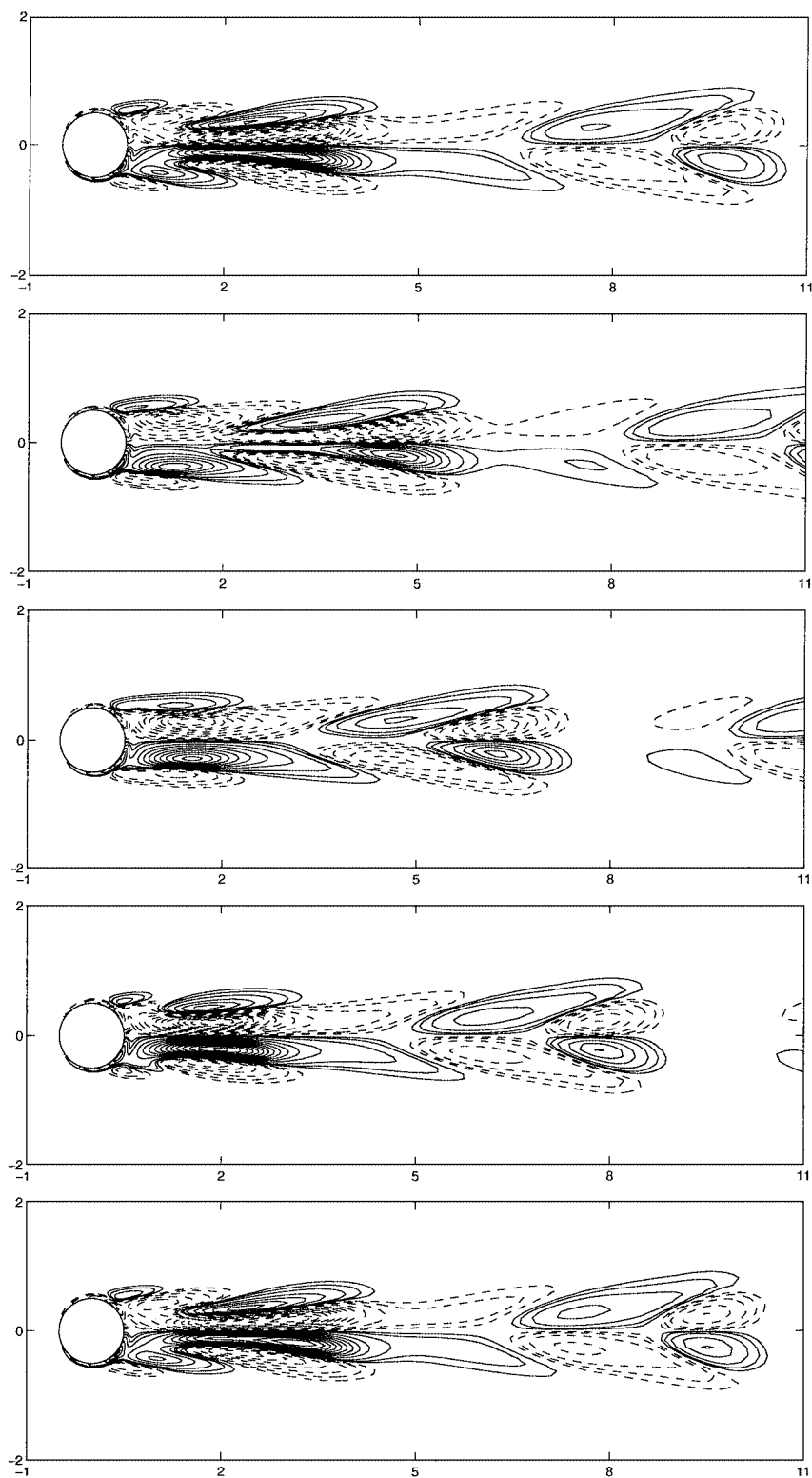


FIG. 8. Flow past a sphere at $Re = 300$. Contours of ω_x in the XZ plane for every quarter period. Levels are by steps of 0.2 (zero level is skipped), with additional contours at ± 0.1 and ± 0.05 .

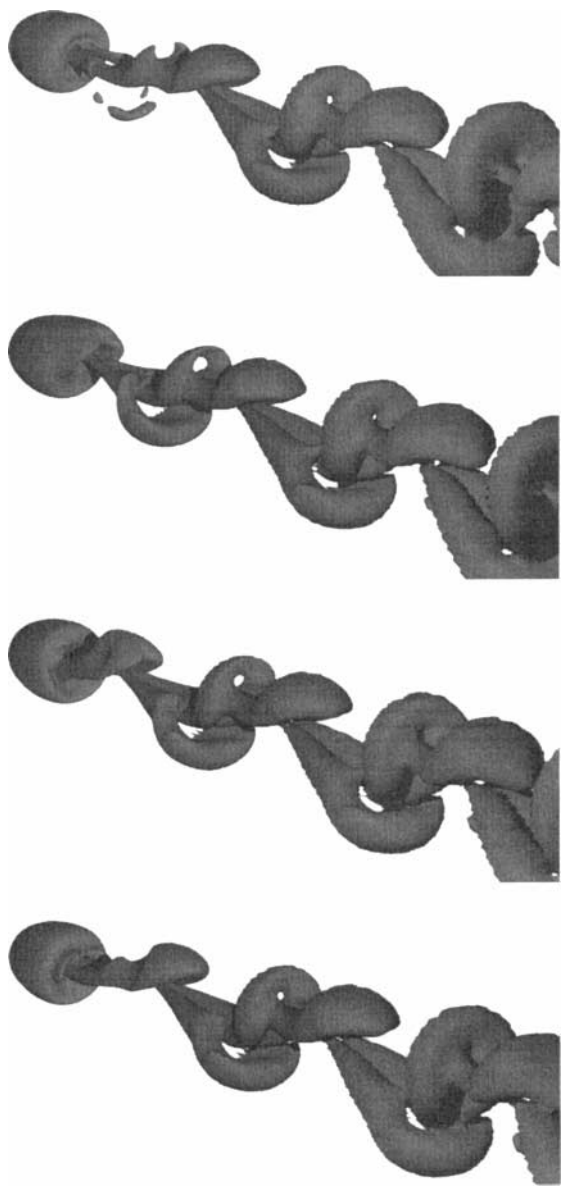


FIG. 9. Flow past a sphere at $Re = 300$. Perspective view of the vorticity structures identified by the λ_2 method, for every quarter period.

definition (51), one has

$$I_x = \frac{1}{2} \int_V (y\omega_z - z\omega_y) dV, \tag{54}$$

$$I_y = \frac{1}{2} \int_V (z\omega_x - x\omega_z) dV. \tag{55}$$

This shows that an error on ω in the far wake induces in turn an error on I_y that is compounded by the x coordinate (that is important in the far wake, and whose average over all particles



FIG. 10. Flow past a sphere at $Re = 300$. XY view (side) and XZ view (top) of the complete extent of the vorticity structures (identified by the λ_2 method) at $T = 75$.

increases in time). Equation (55) also shows that I_x is not affected by this compounding effects, hence the bounded value of C_D predicted by method A.

The mean value of the force coefficients (associated with the time-periodic state of the flow) obtained by Tomboulides [42], Tomboulides and Orszag [43], Johnson [14], and Johnson and Patel [15] is also indicated on Fig. 5. Thus, the two force coefficients become periodic, in good agreement with previous numerical and experimental work (see above).

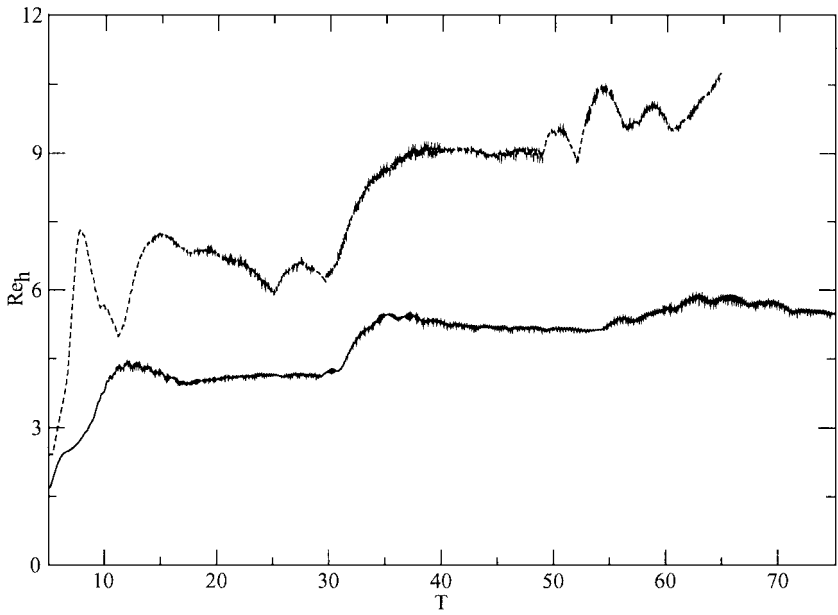


FIG. 11. Flow past a sphere. Maximum “mesh” Reynolds number, $Re_h = \omega h^2/\nu$, as a function of time for $Re = 300$ (solid line) and $Re = 500$ (dashed line).

Computed average values (the average is here taken over the last three cycles) are $\bar{C}_D = 0.683$ and $\bar{C}_L = -0.061$, with oscillation amplitudes $\Delta C_D = (C_{D_{\max}} - C_{D_{\min}})/2 = 2.5 \times 10^{-3}$ and $\Delta C_L = 1.4 \times 10^{-2}$. The Strouhal number is $St = f U_\infty/D = 0.135$. Johnson [14] and Johnson and Patel [15] found $\bar{C}_D = 0.656$, $\bar{C}_L = -0.069$, $\Delta C_D = 3.5 \times 10^{-3}$,

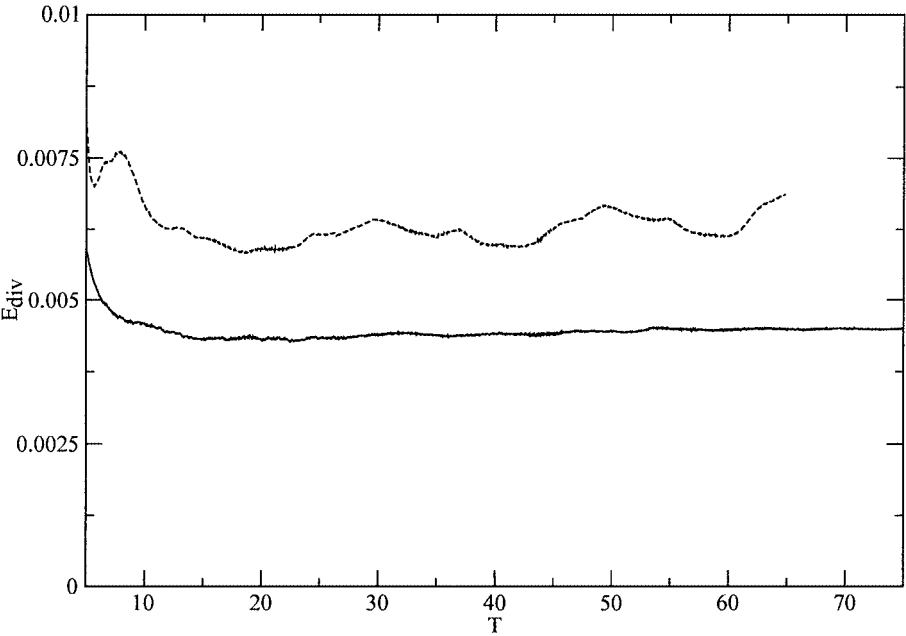


FIG. 12. Flow past a sphere. Divergence error, $E_{\text{div}} = \int_V |\nabla \times \mathbf{u} - \tilde{\omega}|^2 dV / (D U_\infty^2)$, as a function of time, for $Re = 300$ (solid line) and $Re = 500$ (dashed line).

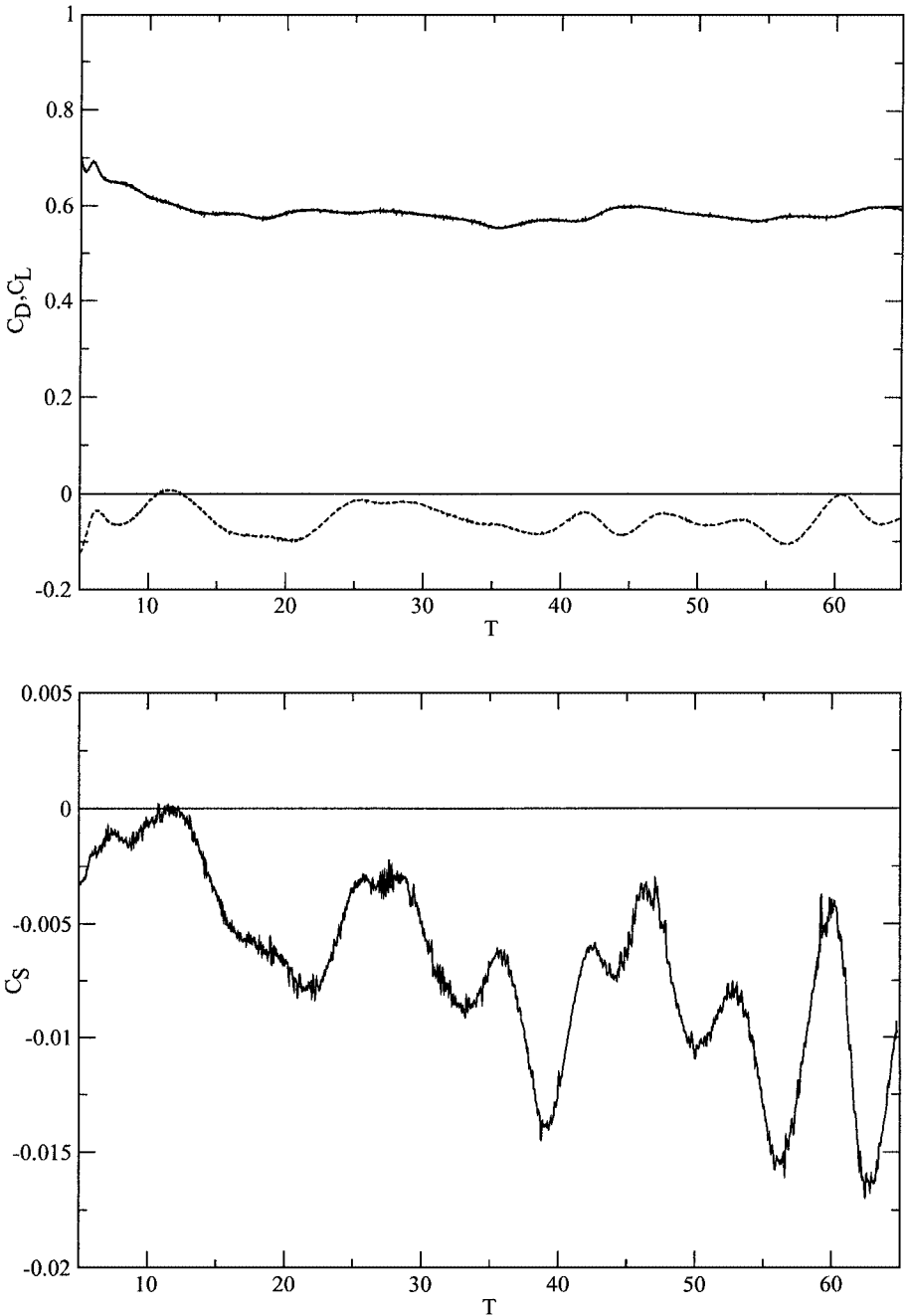


FIG. 13. Flow past a sphere at $Re = 500$. C_D (top, solid line), C_L (top, dashed line), and C_S (bottom) as a function of time.

$\Delta C_L = 1.6 \times 10^{-2}$, and $St = 0.137$. Tomboulides [42] and Tomboulides and Orszag [43] found $\bar{C}_D = 0.671$, $\Delta C_D = 2.8 \times 10^{-3}$, and $St = 0.136$. Our results are thus closer to those of Tomboulides and Orszag than to those of Johnson and Patel. The reason is most likely that the extent of the computational domain of Tomboulides and Orszag ($x_{\max}/D = 25$) is significantly greater than that of Johnson and Patel ($x_{\max}/D = 15$). Hence the influence

of the outflow boundary condition is less important and the results are better. The relative difference between our value of \bar{C}_D and the one of Tomboulides and Orszag is 1.77%. For ΔC_D the relative difference is 11.3%. If one computes the relative difference between the results of Johnson and Patel and those of Tomboulides and Orszag, one finds 2.26 and 22.2% for \bar{C}_D and ΔC_D , respectively. The discrepancies between our results and those of Tomboulides and Orszag are thus smaller than the discrepancies between the results of Tomboulides and Orszag and those of Johnson and Patel.

Contours of ω_z in the near wake XY plane are shown in Fig. 6. The time difference between the pictures is one quarter of a period. A truly periodic regime is attained: The first and the last pictures are basically identical. Contours of ω_y and ω_x in the XZ plane are shown in Figs. 7 and 8. The symmetry of the flow is clearly visible. The λ_2 method of Jeong and Hussain [13] was used to identify the vortex structures. Three-dimensional perspective views for one period are shown in Fig. 9. The complete extent of the wake at the end of the simulations ($T = 75$) is shown in Fig. 10.

Figure 11 shows the maximum “mesh” Reynolds number, $Re_h = |\boldsymbol{\omega}|h^2/\nu$ (with $\boldsymbol{\omega} = \nabla \times \mathbf{u}$), as a function of time. It is seen that Re_h is everywhere smaller than 6. Furthermore, the location where Re_h is greatest is always in the far wake. The flow is thus well resolved in the far wake, and very well resolved near the sphere surface, as $Re_h \simeq 2$ in the boundary layers.

A measure of the vorticity divergence error,

$$\begin{aligned} E_{\text{div}} &= \frac{1}{DU_\infty^2} \int_V |\nabla \times \mathbf{u} - \tilde{\boldsymbol{\omega}}|^2 dV \\ &\simeq \frac{1}{DU_\infty^2} \sum_{i=1}^N |\nabla \times \mathbf{u}(\mathbf{x}_i) - \tilde{\boldsymbol{\omega}}(\mathbf{x}_i)|^2 V_i, \end{aligned} \quad (56)$$

where $\nabla \times \mathbf{u}$ is obtained by analytical differentiation of Eq. (21) (in practice this does not

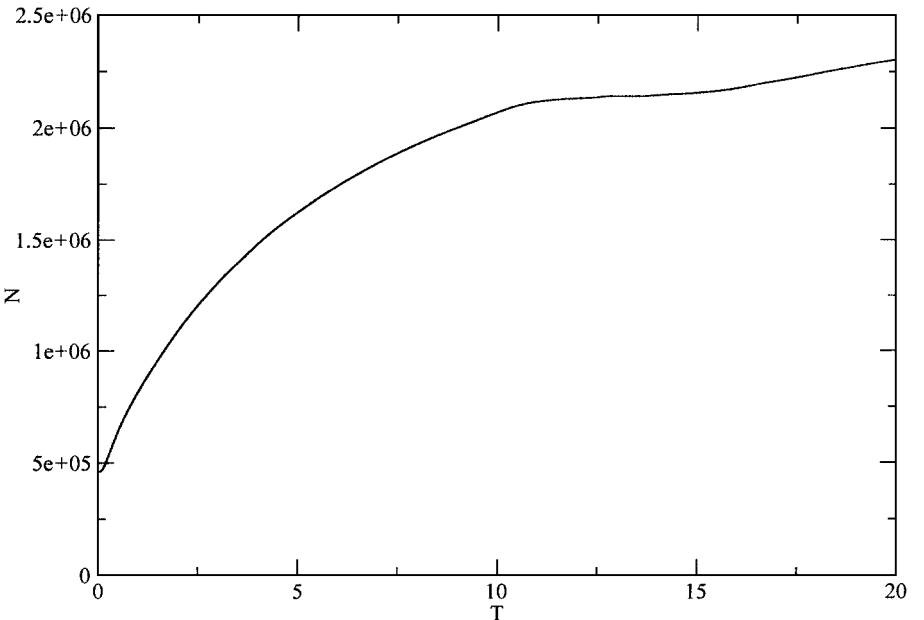


FIG. 14. Flow past a sphere at $Re = 1000$. Number of particles as a function of time.

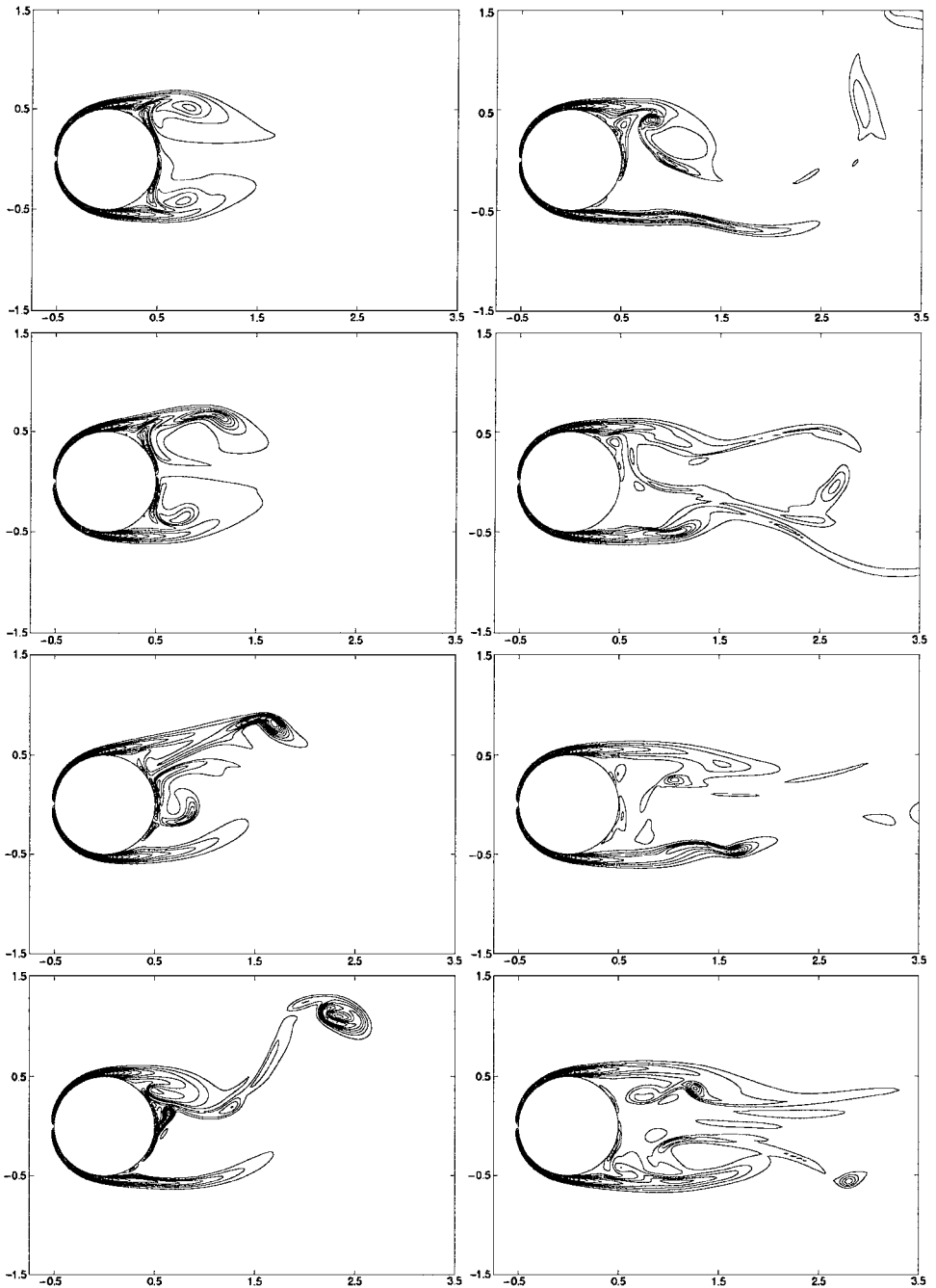


FIG. 15. Flow past a sphere at $Re = 1000$. Contours of $|\omega|$ in the XY plane for $T = 6, 8, 10, 12, 14, 16, 18, 20$ (top to bottom, left to right). Levels are by steps of 2.

imply an extra cost, as the components of the velocity gradient are already computed to account for the stretching term; see Eq. (22)), is shown in Fig. 12. It is higher at the beginning of the simulation (because vortex regions are then very thin, and thus $|\omega|_{\max}$ is large), then decreases and remains roughly constant (as does $|\omega|_{\max}$).

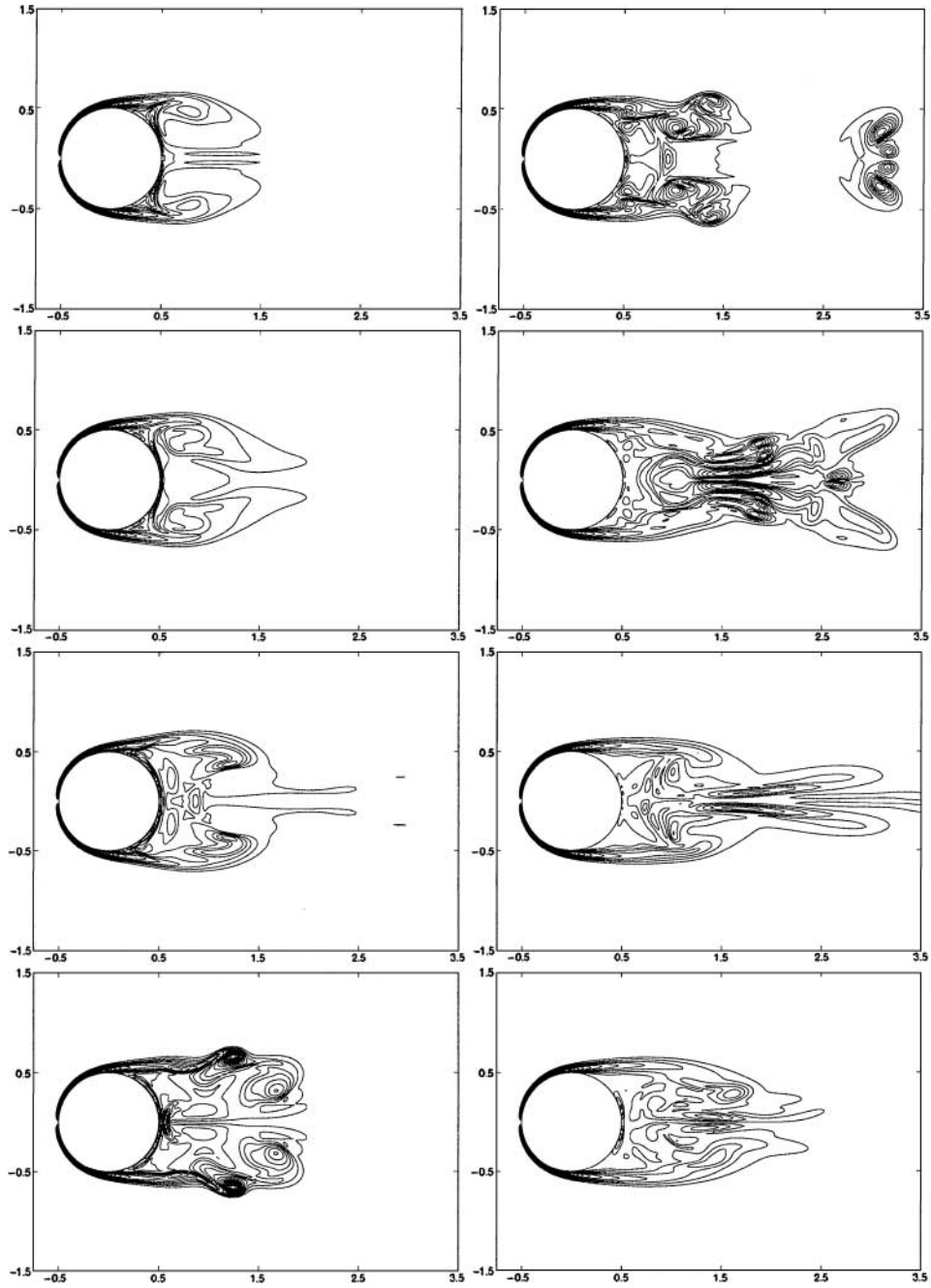


FIG. 16. Flow past a sphere at $Re = 1000$. Contours of $|\omega|$ in the XZ plane for $T = 6, 8, 10, 12, 14, 16, 18, 20$ (top to bottom, left to right). Levels are by steps of 2.

5.2. $Re = 500$

The flow at $Re = 500$ was simulated, using the same perturbation as for the $Re = 300$ case. The time step for the simulation is $\Delta T = 0.01$. The mapping now has $m = 950$. The halo thickness is $d_{\text{halo}}/D = 3.3 \times 10^{-3}$. The control volume has $M_{CV} = 81920$. The

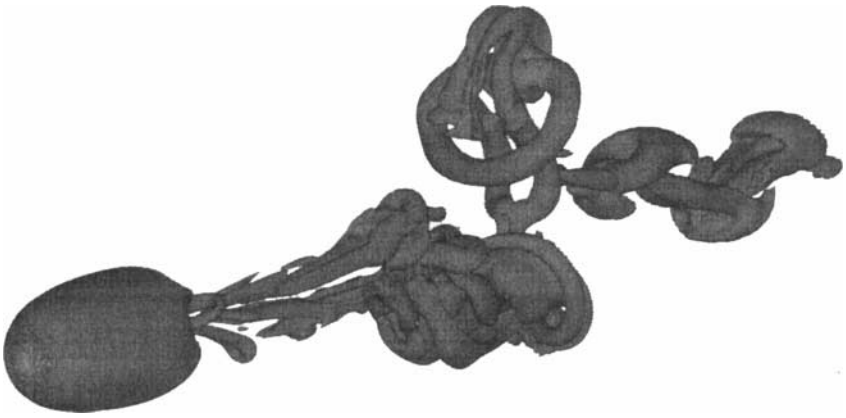


FIG. 17. Flow past a sphere at $Re = 1000$. Perspective view of the vortex structures identified by the λ_2 method, for $T = 20$.

mean error estimate on the norm of the Biot–Savart velocity evaluated at the particles is $\sim 6 \times 10^{-3} U_\infty$. The number of particles increases from $\sim 240,000$ to $\sim 1,225,000$ during the simulation (see Fig. 4). This simulation ran for 1100 h on 32 processors of a Beowulf-type computer made of Pentium Pro running at 200 MHz. Only one particle crossed the body surface during this simulation. The other numerical parameters are identical to those used in Section 5.1.

The drag and lift coefficients (obtained with method B) are reported in Fig. 13. It is seen that they do not become periodic, which is in agreement with the results of Tomboulides [42] and Tomboulides and Orszag [43]. Figure 13 also shows the side force coefficient, $C_S = F_z / ((\frac{1}{2} \rho U_\infty^2)(\pi D^2/4))$, as a function of time. Although no perturbation was

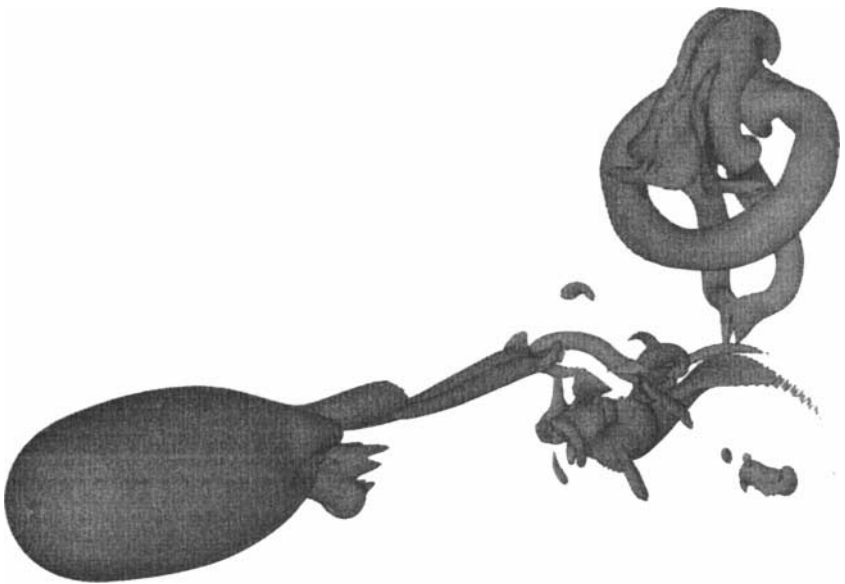


FIG. 18. Flow past a sphere at $Re = 1000$. Perspective view of the isosurface $|\omega| = 2$, for $T = 20$.

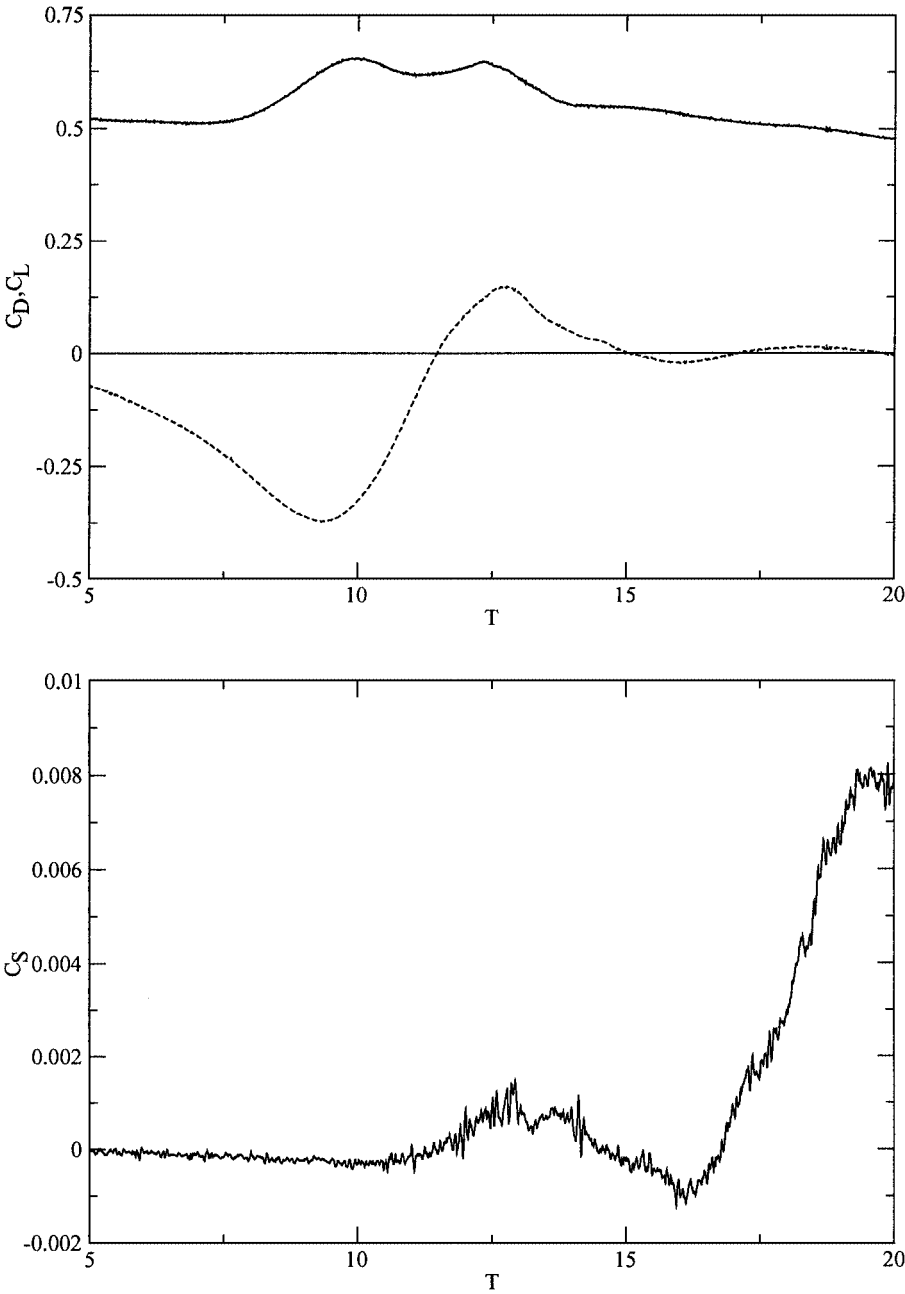


FIG. 19. Flow past a sphere at $Re = 1000$. C_D (top, solid line), C_L (top, dashed line), and C_S (bottom) as a function of time.

introduced in the Z direction, C_S is not zero. This indicates that the flow is becoming fully three dimensional.

The maximum “mesh” Reynolds number as a function of time is shown in Fig. 11. The location where it is maximum is always in the wake, while the boundary layers have $Re_h \simeq 2$. The divergence error, as defined in Eq. (56), is shown in Fig. 12.

5.3. $Re = 1000$

The flow at $Re = 1000$ is now considered. The flow is started impulsively, and a perturbation is applied to trigger the instability: Between $T = 3$ and $T = 4$, the y component of the free-stream velocity is $U_{\infty,y} = 0.1 \sin(\pi(T - 3))$.

The time step for the simulation is $\Delta T = 0.005$. For the mapping, $m = 1350$. The halo thickness is $d_{\text{halo}}/D = 2.3 \times 10^{-3}$, and the number of panels is $M = 81,920$. The mean error estimate on the norm of the Biot–Savart velocity evaluated at the particles is $\sim 6.6 \times 10^{-3} U_{\infty}$. No particles have crossed the body surface during this simulation. The other numerical parameters are as in Section 5.1.

The simulation extends up to $T = 20$. In the course of the computation the number of particles goes from $\sim 460,000$ to $\sim 2,300,000$ (see Fig. 14). The total run time is roughly 230 h on 64 processors of an HP V-Class system.

Contours of $|\omega|$ in the near wake XY and XZ plane are shown in Figs. 15 and 16 for different times. The flow is initially symmetric, as was the perturbation. However, when $T = 18$, the near wake becomes asymmetric (see Fig. 16). This is even clearer at $T = 20$.

Perspective view of the vortex structures (as defined by the λ_2 method) at $T = 20$ is shown in Fig. 17. The surface $|\omega| = 2$ is shown in Fig. 18 (this level corresponds to $\sim 5\%$ of $|\omega|_{\text{max}}$). It is seen that a complex structure, which originates from the perturbation, is shed. This creates significant variations in the drag and lift coefficients, as can be seen in Fig. 19. The side force coefficient, C_S , is also shown in Fig. 19. Although the perturbation was symmetric, the flow is clearly evolving toward a state that is fully three dimensional, i.e., with little or no symmetry. This is supported by Fig. 20, which shows that C_L and C_S are of the same order of magnitude, between $T = 15$ and 20.

The transition to a fully three dimensional flow in the near wake is best seen in Fig. 21, which shows ω_x in the XY plane. The symmetric perturbation did not introduce vorticity in

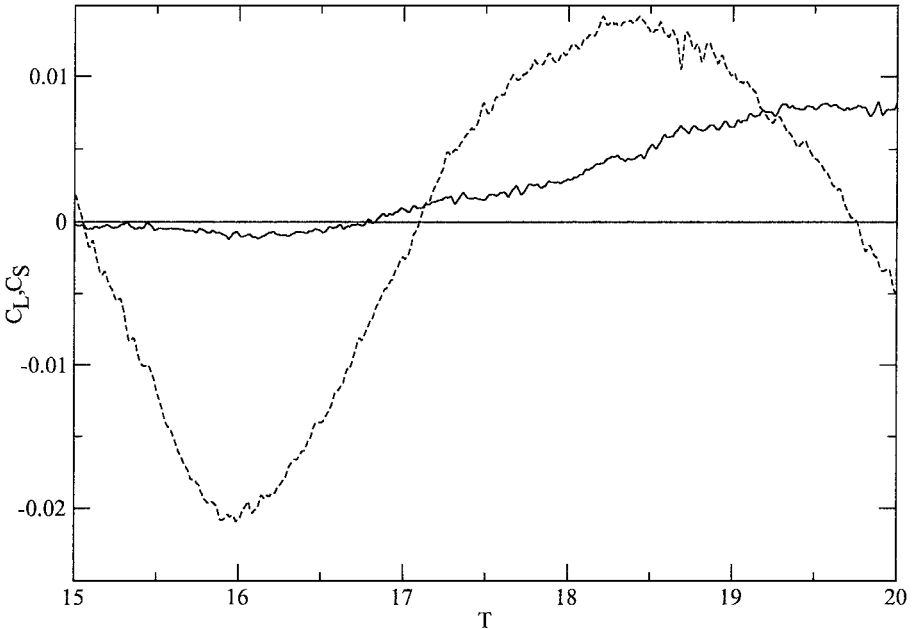


FIG. 20. Flow past a sphere at $Re = 1000$. C_L (solid line) and C_S (dashed line) as a function of time.

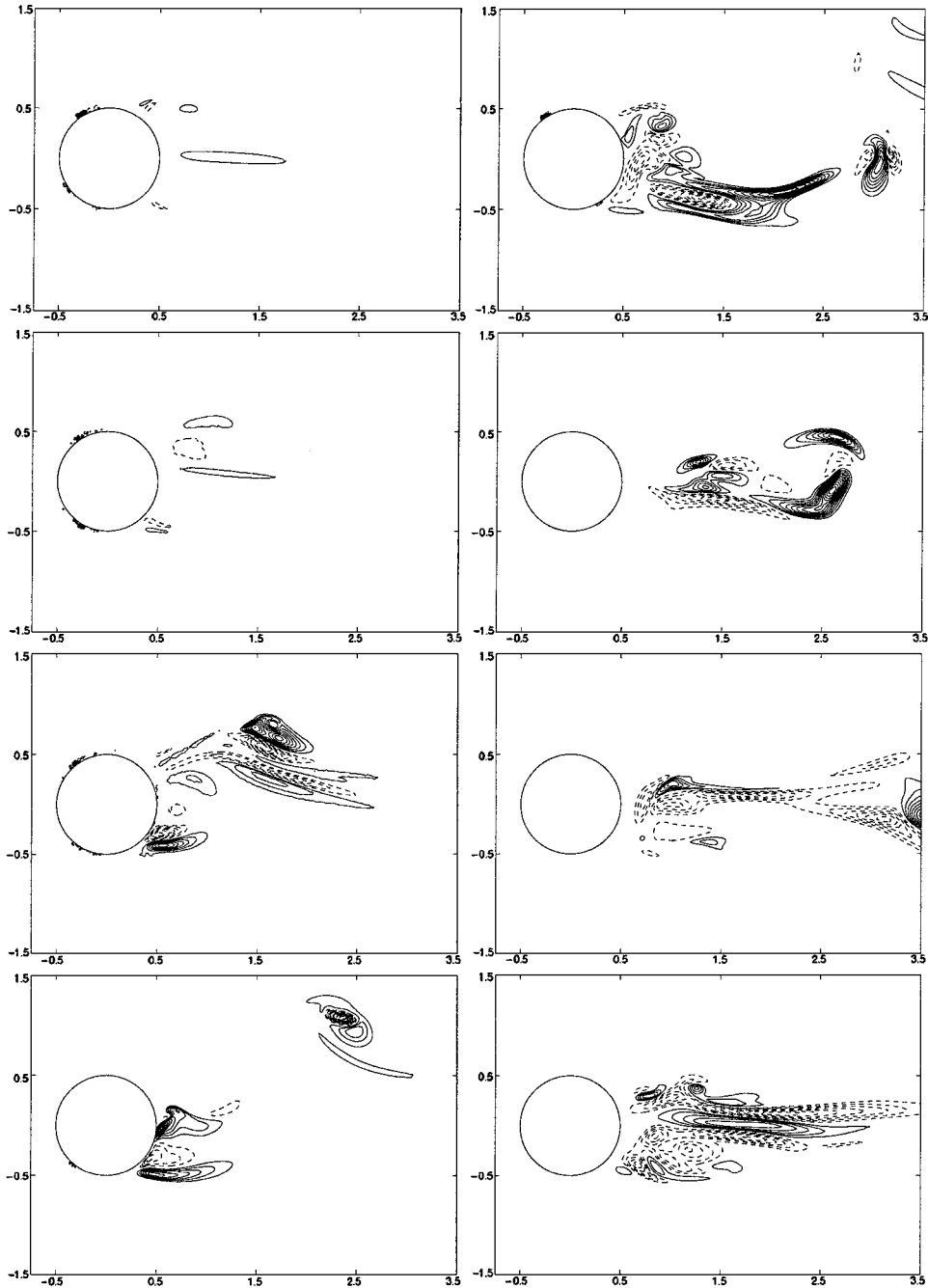


FIG. 21. Flow past a sphere at $Re = 1000$. Contours of ω_x in the XY plane for $T = 6, 8, 10, 12, 14, 16, 18, 20$ (top to bottom, left to right). Levels are by steps of 6.25×10^{-3} for $6 \leq T \leq 10$, 2.5×10^{-2} for $12 \leq T \leq 14$, and 0.4 for $16 \leq T \leq 20$ (zero level is always skipped).

the streamwise direction: Figure 21 indeed confirms that, at $T = 6$, almost no streamwise vorticity exists in the XY plane. At later times, $T = 16\text{--}20$, no ω_x subsists in the regions close to the sphere. Significant ω_x however appears in the near wake, with a magnitude increasing in time: The flow is developing into a truly turbulent flow.

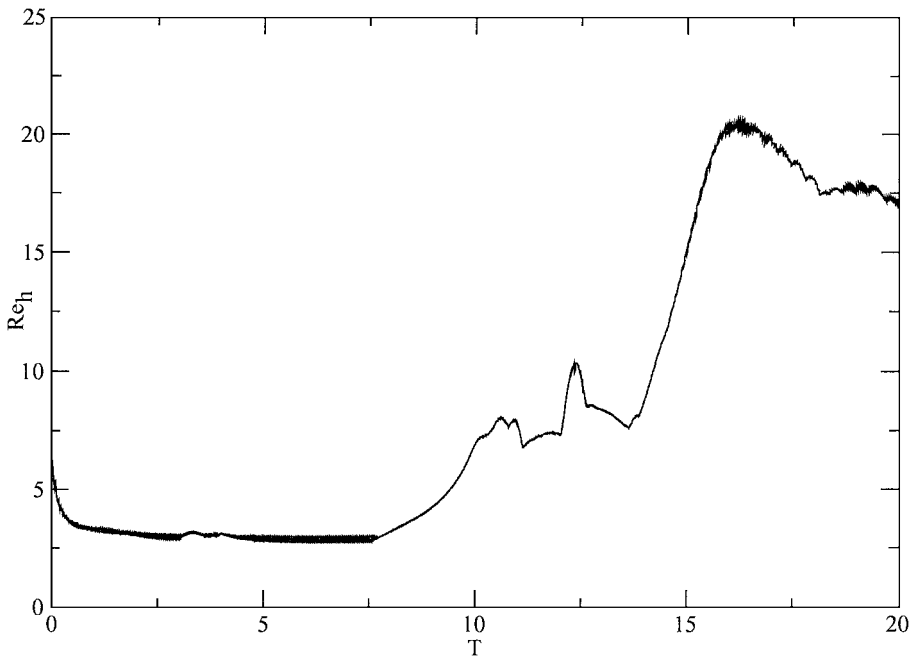


FIG. 22. Flow past a sphere at $Re = 1000$. Maximum mesh Reynolds number, Re_h , as a function of time.

Figure 22 shows the maximum “mesh” Reynolds number, $Re_h = |\boldsymbol{\omega}|h^2/\nu$, as a function of time. It is seen that Re_h is higher than in the simulations for the $Re = 300$ and 500 cases, but an inspection of the numerical data shows that this maximum occurs in the structure that is shed. The flow is still very well resolved near the sphere surface, as $Re_{h,\max} \simeq 3$ in the boundary layers. The divergence error, E_{div} , is reported in Fig. 23.

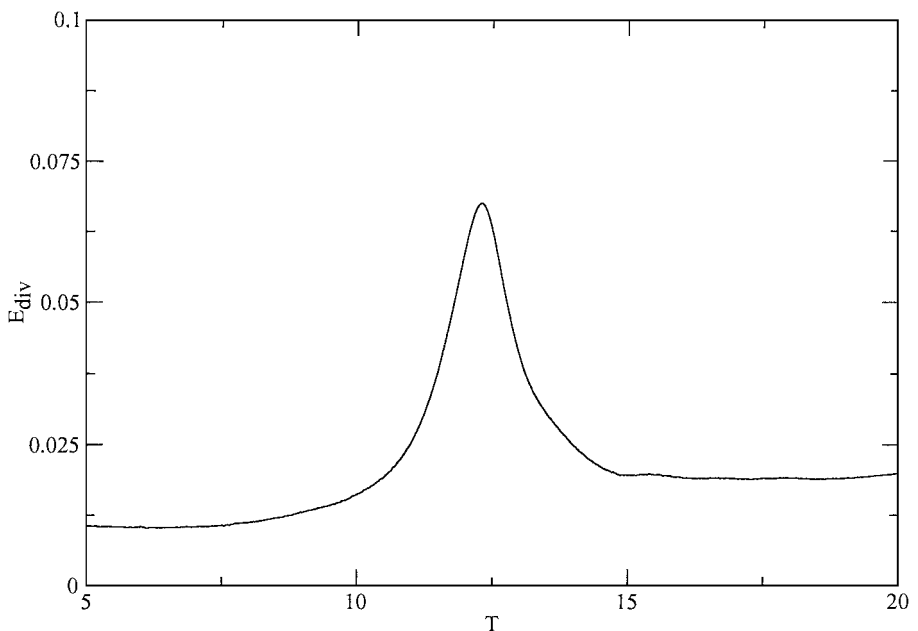


FIG. 23. Flow past a sphere at $Re = 1000$. Divergence error, E_{div} , as a function of time.

6. CONCLUSIONS

Several contributions to the 2-D vortex methods were presented in previous papers [35, 36]. They have been extended to 3-D and combined with previous work on fast parallel tree codes [40, 41, 45–47]. The main feature of the resulting method are as follows:

- A fast parallel tree code is used to compute the velocity and its gradient from the vorticity in $\mathcal{O}(N \log N)$ operations. This allows us to perform simulations with N that is $\mathcal{O}(10^6)$.
- The modified particle strength exchange (PSE) scheme was used near the solid boundaries: It uses images to (a) guarantee a zero flux in the vorticity components parallel to the wall during the PSE substep, and (b) enforce a zero-normal component of the vorticity at the wall.
- The boundary condition is enforced in two steps: A vortex sheet that cancels the slip velocity is first computed; it is then diffused onto nearby particles. The vortex sheet is found as the result of a boundary integral problem that is solved using a parallel iterative solver based on multipole expansions of vortex panels, hence a computational cost of $\mathcal{O}(M \log M)$ per iteration. The scheme used to diffuse the vortex sheet presented herein is a direct extension to 3-D of the scheme presented in previous papers [21, 34–36]. That 2-D scheme was an enhancement of a scheme originally developed by Koumoutsakos *et al.* [17].
- The technique used in [34–36] to redistribute particles in the presence of bodies of general geometry, while conserving the total vorticity, linear impulse and angular impulse, was extended to 3-D.
- A mapping of the redistribution lattice was integrated into the method, making it possible to compute the far wake of bluff-body flows with a coarser, controllable, resolution.
- A method to compute the fluid forces by performing a momentum balance over a control volume, originally developed by Noca *et al.* [30, 31], was modified to only use the velocity and its derivatives on the outer surface of the control volume. This approach makes it possible to compute forces using information from the well-resolved region only.

The 3-D method was validated on the flow past a sphere at $Re = 300$. This flow was computed up to a time of $T = 75$, so that a periodic regime was reached. The mean drag and lift coefficients over one period, as well as the Strouhal number, were shown to be in very good agreement with the results of Tomboulides [42], Johnson [14], Johnson and Patel [15], and Tomboulides and Orszag [43]. The fluctuations' amplitudes of the drag and lift coefficients were in good agreement as well.

The flow past a sphere at $Re = 500$ was computed up to $T = 65$. It did not reach a periodic regime, which is in agreement with previous experimental and numerical work (see Section 5 and references therein). The flow past a sphere at $Re = 1000$ was also computed up to $T = 20$. We intend to further investigate these flows using the present vortex method. The results of the detailed fluid flow analysis will be reported in another paper.

The present vortex method was also used recently to compute flows past other bluff bodies (Brady, private communication, 2000): a rounded cube, two rounded cubes in tandem, rounded prisms, a rounded cube above a viscous ground.

A possible way to speed up the vortex method would be to couple the multipole method we use with vortex-in-cell methods: The multipole Poisson solver would then be used to obtain the boundary condition required by the grid-based Poisson solver, thereby allowing use of a grid bounding the vortical region very tightly. This coupled approach seems promising and we intend to investigate it in the future.

ACKNOWLEDGMENTS

P. Ploumhans was supported by the Fonds pour la Formation à la Recherche dans l'Industrie et dans l'Agriculture (FRIA), and by the FSR (Fonds Spéciaux de Recherche) of UCL. The research was also supported by NSF cooperative agreement ACI-9619020 through computing resources provided by the National Partnership for Advanced Computational Infrastructure at the Caltech Center for Advanced Computing Research (CACR). Additional time on the V-Class system was provided by CACR. Access to the Pentium Pro-based Beowulf cluster (naegling), located at Caltech, was also provided by CACR. Postprocessing of the results was done, in part, using tools developed by M. A. Brady. Perspective views in Sections 5.1 and 5.2 were produced using the "Persistence of Vision" ray tracing program (*povray*). Those in Section 5.3 were produced with the Parallel Graphics Library (PGL) developed by T. W. Crockett at the Institute for Computer Applications in Science and Engineering.

REFERENCES

1. M. Bar-Lev and H. T. Yang, Initial flow field over an impulsively started circular cylinder, *J. Fluid Mech.* **72**, 625 (1975).
2. J. E. Barnes and P. Hut, A hierarchical $\mathcal{O}(N \log N)$ force calculations algorithm, *Nature* **324**, 446 (1986).
3. J. T. Beale, On the accuracy of vortex methods at large times, in *Proc. Workshop on Comput. Fluid Dyn. and React. Gas Flows, IMA, Univ. of Minnesota, 1986*, edited by B. Engquist *et al.* (Springer-Verlag, New York, 1988), p. 19.
4. R. Benhaddouch, Treatment of Neumann boundary condition by a particle strength exchange method, in *Proc. Third International Workshop on Vortex Flows and Related Numerical Methods, Toulouse, France, August 24–27, 1998*, ESAIM (European Series in Applied and Industrial Mathematics) (1999), available at <http://www.emath.fr/Maths/Proc/Vol.7/>.
5. G.-H. Cottet, On 3D vortex schemes, in *Proc. 1996 ASME Fluids Engineering Division Summer Meeting, San Diego, CA, July 7–11, 1996*, ASME FED, edited by H. Coleman *et al.* (ASME, New York, 1996), Vol. 238, 135–140.
6. G.-H. Cottet, M. L. Ould Salihi, and M. El Hamraoui, Multi-purpose regridding in vortex methods, in *Proc. Third International Workshop on Vortex Flows and Related Numerical Methods, Toulouse, France, August 24–27, 1998*, ESAIM (European Series in Applied and Industrial Mathematics) (1999), available at <http://www.emath.fr/Maths/Proc/Vol.7/>.
7. G.-H. Cottet and P. Koumoutsakos, *Vortex Methods: Theory and Applications* (Cambridge Univ. Press, Cambridge, UK, 2000).
8. G.-H. Cottet, P. Koumoutsakos, and M. L. Ould Salihi, Vortex methods with spatially varying cores, *J. Comput. Phys.* **162**, 164 (2000).
9. P. Degond and S. Mas-Gallic, The weighted particle method for convection–diffusion equations. I: The case of an isotropic viscosity. II: The anisotropic case, *Math. Comput.* **53**, 485 (1989).
10. J. D. Eldredge, A. Leonard, and T. Colonius, A general deterministic treatment of derivatives in particle methods, *J. Comput. Phys.*, to appear.
11. L. Greengard and V. Rohklin, A fast algorithm for particle simulations, *J. Comput. Phys.* **73**, 325 (1987).
12. O. H. Hald, Convergence of vortex methods for Euler's equations II, *SIAM J. Numer. Anal.* **16**, 726 (1981).
13. J. Jeong and F. Hussain, On the identification of a vortex, *J. Fluid Mech.* **285**, 69 (1995).
14. T. A. Johnson, *Numerical and Experimental Investigation of Flow past a Sphere up to a Reynolds Number of 300*, Ph.D. thesis (The University of Iowa, Iowa City, IA, 1996).
15. T. A. Johnson and V. C. Patel, Flow past a sphere up to a Reynolds number of 300, *J. Fluid Mech.* **378**, 19.
16. P. Koumoutsakos, *Direct Numerical Simulations of Unsteady Separated Flows Using Vortex Methods*, Ph.D. thesis (California Institute of Technology, Pasadena, CA, 1993).
17. P. Koumoutsakos, A. Leonard, and F. Pépin, Boundary conditions for viscous vortex methods, *J. Comput. Phys.* **113**, 52 (1994).
18. P. Koumoutsakos and A. Leonard, High resolution simulation of the flow around an impulsively started cylinder using vortex methods, *J. Fluid Mech.* **296**, 1 (1995).

19. P. Koumoutsakos and D. Shiels, Simulations of the viscous flow normal to an impulsively started and uniformly accelerated flat plate, *J. Fluid Mech.* **328**, 177 (1996).
20. P. Koumoutsakos, Inviscid axisymmetrization of an elliptical vortex, *J. Comput. Phys.* **138**, 821 (1997).
21. A. Leonard, D. Shiels, J. K. Salmon, G. S. Winckelmans, and P. Ploumhans, Recent advances in high resolution vortex methods for incompressible flows, in *Proc. 13th AIAA Computational Fluid Dynamics Conf., Snowmass Village, CO, June 29–July 2, 1997*, AIAA paper 97-2108, pp. 1–17 (1997).
22. A. Leonard, Review: Vortex methods for flow simulation, *J. Comput. Phys.* **37**, 289 (1980).
23. A. Leonard, Computing three-dimensional incompressible flows with vortex elements, *Annu. Rev. Fluid Mech.* **17**, 523 (1985).
24. E. Levi, Three-dimensional wakes: Origin and evolution, *J. Eng. Mech.* **106**, 659 (1980).
25. R. H. Magarvey and R. L. Bishop, Wakes in liquid–liquid systems, *Phys. Fluids* **4**, 800 (1961).
26. R. H. Magarvey and R. L. Bishop, Vortices in sphere wake, *Can. J. Phys.* **43**, 1649 (1965).
27. S. Mas-Gallic, Particle approximation of a linear convection-diffusion problem with Neumann boundary conditions, *SIAM J. Num. Anal.* **32**(4), 1098 (1995).
28. R. Mittal, Planar symmetry in the unsteady wake of a sphere, *AIAA J.* **37**(3), 388 (1998).
29. R. Natarajan and A. Acrivos, The instability of the steady flow past spheres and disks, *J. Fluid Mech.* **254**, 323 (1993).
30. F. Noca, D. Shiels, and D. Jeon, Measuring instantaneous fluid dynamic forces on bodies using only velocity fields and their derivatives, *J. Fluids Struct.* **11**, 345 (1997).
31. F. Noca, D. Shiels, and D. Jeon, A comparison of methods for evaluating time-dependent fluid dynamic forces on bodies using only velocity fields and their derivatives, *J. Fluids Struct.* **13**, 551 (1999).
32. M. L. Ould Salih, *Couplage de Méthodes Numériques en Simulation Directe d'Écoulements Incompressibles*, Thèse (Université Joseph Fourier, Grenoble, France, 1998).
33. D. Ormières and M. Provansal, Transition to turbulence in the wake of a sphere, *Phys. Rev. Lett.* **83**(1), 80 (1999).
34. P. Ploumhans, G. S. Winckelmans, and J. K. Salmon, Vortex particles and tree codes. I. Flows with arbitrary crossing between solid boundaries and particle redistribution lattice. II. Vortex ring encountering a plane at an angle, in *Proc. Third International Workshop on Vortex Flows and Related Numerical Methods, Toulouse, France, August 24–27, 1998*, ESAIM (European Series in Applied and Industrial Mathematics) (1999), available at <http://www.emath.fr/Maths/Proc/Vol.7/>.
35. P. Ploumhans and G. S. Winckelmans, Vortex methods for high resolution simulations of viscous flow past bluff-bodies of general geometry, *J. Comput. Phys.* **165**, 354 (2000).
36. P. Ploumhans and G. S. Winckelmans, Vortex methods for high resolution simulations of viscous flow past bluff-bodies of general geometry, Erratum, *J. Comput. Phys.* **170**, 449 (2001).
37. P. G. Saffman, *Vortex Dynamics* (Cambridge Univ. Press, Cambridge, UK, 1992).
38. H. Sakamoto and H. Haniu, A study of vortex shedding from spheres in a uniform flow, *Trans. ASME J. Fluids Eng.* **112**, 386 (1990).
39. H. Sakamoto and H. Haniu, The formation mechanism and shedding frequency of vortices from a sphere in uniform shear flow, *J. Fluid Mech.* **287**, 151 (1995).
40. J. K. Salmon and M. S. Warren, Skeletons from the treecode closet, *J. Comput. Phys.* **111**, 136 (1994).
41. J. K. Salmon, M. S. Warren, and G. S. Winckelmans, Fast parallel treecodes for gravitational and fluid dynamical N-body problems, *Int. J. Supercomput. Appl.* **8**, 129 (1994).
42. A. G. Tomboulides, *Direct and Large-Eddy Simulation of Wake Flows: Flow past a Sphere*, Ph.D. thesis (Princeton University, Princeton, NJ, 1993).
43. A. G. Tomboulides and S. A. Orszag, Numerical investigation of transitional and weak turbulent flow past a sphere, *J. Fluid Mech.* **416**, 45 (2000).
44. G. S. Winckelmans and A. Leonard, Contributions to vortex particle methods for the computation of three-dimensional incompressible unsteady flows, *J. Comput. Phys.* **109**, 247 (1993).
45. G. S. Winckelmans, J. K. Salmon, A. Leonard, and M. S. Warren, Three-dimensional vortex particle and panels methods: Fast tree-code solvers with active error control for arbitrary distributions/geometries, in *Proc. Forum*

- on Vortex Methods for Engineering Applications, Albuquerque, NM, February 22–24, 1995* (sponsored by Sandia National Laboratories), p. 25.
46. G. S. Winckelmans, J. K. Salmon, M. S. Warren, and A. Leonard, The fast solution of three-dimensional fluid dynamical N-body problems using parallel tree codes: Vortex element method and boundary element method, in *Proc. Seventh SIAM Conference on Parallel Processing for Scientific Computing, San Francisco, CA, Feb. 15–17, 1995* (SIAM, Philadelphia, PA, 1995), p. 301.
 47. G. S. Winckelmans, J. K. Salmon, M. S. Warren, A. Leonard, and B. Jodoin, Application of fast parallel and sequential tree codes to computing three-dimensional flows with the vortex element and boundary element methods, in *Proc. Second International Workshop on Vortex Flows and Related Numerical Methods, Montréal, Canada, August 20–24, 1995*, ESAIM (European Series in Applied and Industrial Mathematics) (1997), available at <http://www.emath.fr/Maths/Proc/Vol.1/index.htm>.
 48. J. S. Wu and G. M. Faeth, Sphere wakes in still surroundings at intermediate Reynolds numbers, *AIAA J.* **31**, 1448 (1993).